

DOKUZ EYLÜL UNIVERSITY
GRADUATE SCHOOL OF NATURAL AND APPLIED
SCIENCES

FINITE ELEMENT METHOD AND
STEP-BY-STEP PERTURBATION METHOD FOR
HIGH FREQUENCY EIGENVALUE PROBLEMS

by
Mehmet Mert TAYGUR

June, 2014

İZMİR

FINITE ELEMENT METHOD AND STEP-BY-STEP PERTURBATION METHOD FOR HIGH FREQUENCY EIGENVALUE PROBLEMS

**A Thesis Submitted to the
Graduate School of Natural and Applied Sciences of Dokuz Eylül University
In Partial Fulfillment of the Requirements for the Degree of Master of Science
in Electrical and Electronics Engineering Program**

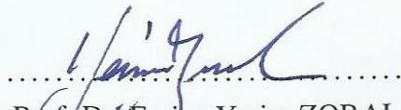
**by
Mehmet Mert TAYGUR**


June, 2014


İZMİR

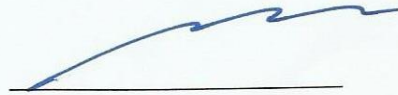
M.Sc THESIS EXAMINATION RESULT FORM

We have read the thesis entitled "FINITE ELEMENT METHOD AND STEP-BY-STEP PERTURBATION METHOD FOR HIGH FREQUENCY EIGENVALUE PROBLEMS" completed by MEHMET MERT TAYGUR under supervision of PROF. DR. EMİNE YEŞİM ZORAL and we certify that in our opinion it is fully adequate, in scope and in quality, as a thesis for the degree of Master of Science.


.....
Prof. Dr. Emine Yeşim ZORAL


.....
Prof. Dr. Valery YAKUBOV


.....
Assoc. Prof. Dr. Serkan GÜNEC


.....

Prof. Dr. Ayşe OKUR

Director

Graduate School of Natural and Applied Sciences

ACKNOWLEDGEMENTS

My sincere gratitude,
To my family for their endless support,
To my dear Yaprak, for her companionship,
and to Yeşim Zoral and Serkan Günel for their guidance and kindness,

This work has been supported by The Scientific and Technological Research Council of Turkey (TUBITAK) under Grant No. 111E059.

Mehmet Mert TAYGUR

FINITE ELEMENT METHOD AND STEP-BY-STEP PERTURBATION METHOD FOR HIGH FREQUENCY EIGENVALUE PROBLEMS

ABSTRACT

Cavity resonators are widely employed passive components in microwave applications, such as oscillators, amplifiers and filters, due to their simple geometries and high quality factors in general. Perturbation of these structures by a small object or changing the geometry slightly, has been studied for a long time since the perturbation analysis can be critical for tuning and optimization applications. When the perturbation is small, classical perturbation techniques work well. On the other hand, for the problems where analytical solutions do not exist or the amount of perturbation is relatively large, numerical techniques, such as finite element method, must be utilized. Analysis of the resonant structures using finite element method, corresponds to a generalized eigenvalue-eigenvector problem. Resulting eigenvalues and eigenvectors provide information about the resonant frequencies and the field intensities of the corresponding modes, respectively. For the optimization and tuning processes, it is useful to extract a parametric history information. However, this operation requires successive finite element operations which is time consuming. Especially for the applications where large variations are demanded, the step-by-step perturbation technique can be used. In this study, the material perturbation of a cubic resonant cavity is investigated by combining the step-by-step perturbation technique and nodal finite element method. The required software is created using Python scripting language. The results produced by this software is compared with Ansoft HFSS and the analytical solutions where possible.

Keywords: Finite element method, step-by-step perturbation, eigenvalue eigenvector problem, cubic resonant cavity, parametric history

SONLU ELEMANLAR VE ADIM-ADIM PERTÜRBASYON YÖNTEMİNİN YÜKSEK FREKANS ÖZDEĞER PROBLEMLERİNE UYGULANMASI

ÖZ

Basit geometrileri ve yüksek kalite faktörleri nedeniyle, kavite rezonatörler, osilatör, yükseltici ve süzgeç gibi mikrodalga uygulamalarında yaygın olarak kullanılırlar. Bu yapıların pertürbasyon çözümlemesi optimizasyon ve ince ayar uygulamalarında kritik olduğu için, içlerine küçük bir obje sokulması ve/veya geometrilerinin hafifçe değiştirilmesiyle yapılan pertürbasyonların çözümlemeleri uzunca bir süredir araştırılmaktadır. Pertürbasyon miktarının küçük olduğu durumlarda, klasik pertürbasyon yöntemleri iyi sonuç vermektedir. Öte yandan, analitik çözümün mümkün olmadığı veya pertürbasyon miktarının görece yüksek olduğu durumlarda, sonlu elemanlar yöntemi gibi nümerik metodlar kullanılmalıdır. Rezonans yapılarının sonlu elemanlar metodu ile çözümlenmesi, genelleştirilmiş özdeğer-özvektör problemine karşılık gelir. Elde edilen özdeğer ve özvektörler, rezonans frekansları ve bunlara karşılık gelen modların alan şiddetleriyle ilgili bilgi verir. Optimizasyon ve ince ayar süreçleri için, parametrik geçmiş bilgisi çıkarmak faydalıdır. Fakat bu işlem ardışıl sonlu elemanlar çözümlemesi gerektirir ki bu da zaman alıcıdır. Özellikle büyük değişimler gerektiği zaman, adım adım pertürbasyon tekniği kullanılabilir. Bu çalışmada, kübik bir rezonans kavitesinin malzeme pertürbasyonu, adım adım pertürbasyon tekniği ve düğüm tabanlı sonlu elemanlar yöntemi tümleştirilerek incelenmiştir. Bu amaca uygun olarak geliştirilen yazılım, Python programlama dili ile oluşturulmuştur. Bu yazılımla elde edilen sonuçlar, Ansoft HFSS ve analitik çözümlerle karşılaştırılmıştır.

Anahtar kelimeler: Sonlu elemanlar yöntemi, adım-adım pertürbasyon, özdeğer-özvektör problemi, kübik rezonans kavitesi, parametrik geçmiş çözümlemesi

CONTENTS

	Page
THESIS EXAMINATION RESULT FORM	ii
ACKNOWLEDGEMENTS	iii
ABSTRACT.....	iv
ÖZ	v
CONTENTS	vi
LIST OF FIGURES	viii
LIST OF TABLES.....	x
 CHAPTER ONE - INTRODUCTION.....	 1
1.1 Motivation	1
1.2 Thesis Structure	3
 CHAPTER TWO - ELECTROMAGNETIC RESONANCE PROBLEM	 4
2.1 Analytical Solution For Cubic Cavity	5
2.1.1 Uniformly Filled Cubic Cavity	5
2.1.2 Partially Filled Cubic Cavity.....	8
2.2 Cavity Problems without Analytical Solutions	12
 CHAPTER THREE - EIGENVALUE PROBLEMS IN FINITE ELEMENT METHOD.....	 14
3.1 Finite Element Method	14
3.1.1 General Finite Element Method Formulation.....	14
3.1.2 Finite Element Formulation For Rectangular Cavity	17
3.1.3 Spurious Modes	20
3.2 Step-By-Step Eigenvalue Perturbation Technique For Resonant Cavity Structures	20
3.2.1 Classical Eigenvalue Perturbation Method	21
3.2.2 Step-by-Step Eigenvalue Perturbation Method.....	22

CHAPTER FOUR - SOFTWARE DEVELOPMENT AND NUMERICAL RESULTS	24
4.1 Software Development	24
4.1.1 FEM Routine	24
4.1.2 Step-By-Step Perturbation Routine	27
4.1.3 GUI	28
4.1.4 Future Work For Software.....	30
4.2 Numerical Results	31
4.2.1 FEM Results	31
4.2.1.1 Mesh Resolution.....	32
4.2.1.2 Divergence Coefficient.....	33
4.2.2 Step-By-Step Eigenvalue Perturbation Results.....	41
4.2.2.1 Number of Perturbation Steps.....	42
4.2.2.2 Eigenvalue Identification & Perturbation Interval	43
4.2.2.3 Number of Eigenvalues	45
4.2.2.4 Effects of Spurious Solutions.....	47
 CHAPTER FIVE - CONCLUSION	 53
 REFERENCES	 57

LIST OF FIGURES

	Page
Figure 2.1 A cylindrical cavity	4
Figure 2.2 Partially filled cavity illustration	8
Figure 2.3 Magnetic field illustrations of an empty (left) and a partially filled cavity (right).....	12
Figure 2.4 An empty rectangular cavity with a pill-shaped dielectric material....	12
Figure 3.1 (a) A tetrahedral element (b) Discretization of a cube with tetrahedral elements	15
Figure 4.1 Gmsh GUI	25
Figure 4.2 FEM routine flowchart for an eigenvalue problem.....	26
Figure 4.3 GUI control panel of the created software	28
Figure 4.4 FEM and perturbation result windows of the created software	29
Figure 4.5 Magnetic field components (H_x , H_y , H_z) for $10 \times 10 \times 10$ mm cubic cavity.....	30
Figure 4.6 First 20 eigenvalues found by FEM routine for the tetrahedral characteristic lengths (a) 5mm (b) 2mm (c) 1mm (d) 0.75mm	33
Figure 4.7 Magnetic field intensity plot from Ansoft HFSS for cubic cavity.....	34
Figure 4.8 Resonant frequencies for a cubic cavity ($10 \times 10 \times 10$ mm, $\epsilon_r = 1$) between 20-25 GHz for $s=0$	35
Figure 4.9 The field plots of H_x , H_y , H_z for $s=0$ at 21.5239 GHz.....	36
Figure 4.10 The smallest eigenvalues for $s=0.5$	36
Figure 4.11 The magnetic field intensity plot for $s=0.5$ at 21.9117 GHz.....	37
Figure 4.12 The magnetic field intensity plots of 6 eigenvalues near 21.5 GHz for $s=1$	38
Figure 4.13 The smallest eigenvalues for $s=1.5$	39
Figure 4.14 The field plots of the modes for $s=1.5$ near 22.5 GHz	39
Figure 4.15 The smallest eigenvalues for $s=1.5$, characteristic length=0.75mm ...	40
Figure 4.16 Perturbation analysis of the partially filled cavity by (a) 80 steps (b) 20 steps (c) 5 steps, from $\epsilon_{r2}=4$ to 1	43
Figure 4.17 Perturbation analysis from $\epsilon_{r1}=1$ to $\epsilon_{r2}=4$, 10 by 5, 20 steps	44
Figure 4.18 Deflection of eigenvalues during the perturbation process.....	45
Figure 4.19 Variation and deflection of nine eigenvalues during the perturbation process	45
Figure 4.20 Effects of number of initial eigenvalues for (a) 20 (b) 80 , ϵ_{r2} is perturbed from 4 to 1.....	46

Figure 4.21	Effects of number of initial eigenvalues for (a) 20 (b) 80, ϵ_{r_2} is perturbed 1 to 4	46
Figure 4.22	Effects of number of initial eigenvalues for (a) 20 (b) 80, ϵ_{r_2} is perturbed 1 to 10	46
Figure 4.23	FEM errors calculated by (a) Point-wise energy (b) Energy density (c) Divergence for the elimination of the spurious modes	49
Figure 4.24	Errors of 25 modes without spurious exclusion calculated by (a) Point-wise energy (b) Energy density (c) Divergence obtained from perturbation	51
Figure 4.25	Errors of 25 modes with spurious exclusion calculated by (a) Point-wise energy (b) Energy density (c) Divergence obtained from perturbation	52

LIST OF TABLES

	Page
Table 2.1 Resonant frequency comparison for cubic cavity.....	7
Table 4.1 SciPy eigenvalue algorithms benchmark	27
Table 4.2 First 12 resonant frequencies of a cubic cavity with $10 \times 10 \times 10$ mm, $\epsilon_r = 1$	31
Table 4.3 Lowest 12 resonant frequencies of a $10 \times 10 \times 10$ mm, $\epsilon_r = 1$ cavity found by HFSS.....	34
Table 4.4 Lowest 12 resonant frequencies of a $10 \times 10 \times 10$ mm, $\epsilon_{r_1} = 1$, $\epsilon_{r_2} = 4$ partially filled cavity	41
Table 4.5 Lowest 21 resonant frequencies of the partially filled cavity obtained from HFSS	42

CHAPTER ONE

INTRODUCTION

1.1 Motivation

Microwave resonators have been widely used components for RF oscillator and amplifier circuits. They can be in various forms such as metallic cavity, planar microstrip or circuit with lumped components. Design and analysis of these structures became easier with the improvements in the numerical methods and the computing power. Cavity resonators are favorable in this manner due to the relative ease in construction and high quality factor.

Perturbation of the resonant cavities has been studied for several decades, hence it is possible to find numerous application examples such as material measurement, tuning and optimization. Earlier studies were mostly focused on the analytical formulation of the Maxwells' equations when a small object is inserted into the cavity or the dimensions were altered (Spencer et al., 1957; Price et al., 1963). It is well known that the classical perturbation method works well when the amount of perturbation is relatively small. However, depending on the application, this condition may not always be satisfied. In this case, the solution of the problem can be obtained using approximate methods (Zaki & Atia, 1983; Carter, 2001). It should be noted that though, these formulas are applicable for a few specific case only, since most of the problems couldn't be solved analytically. The solution of such problems have been feasible with the arise of the numerical methods, such as the finite element method (FEM).

Earlier examples of FEM was based on nodal discretization where the field components are solved at discrete nodal points of the geometrical structure. This procedure caused some non-physical, spurious solutions to occur for waveguide and cavity problems. Various methods to deal with the spurious modes have been proposed, such as penalty term method (Rahman & Davies, 1984), but none of them have been as effective as the development of the vector FEM, where edge based elements are used instead of nodal ones. Removal of the spurious solutions have been a major improvement for the finite element analysis of the waveguides and cavities, as a result, many different problems have been investigated thoroughly (Wang & Ida, 1992; Lee & Mittra, 1992). This also caused the commercial FEM software to arise and simplified the design and analysis of electromagnetic systems. Nevertheless, nodal

FEM hasn't declined completely due to easier discretization compared to the edge-based FEM which requires complex geometrical algorithms and data management for discretization. Computational requirements of the FEM routines have always been higher, compared to the other aspects though, since the analysis of the cavity problem by means of FEM requires the solution of a generalized eigenvalue/eigenvector problem which may include several thousand variables. Optimization, sensitivity analysis or fine-tuning of the cavity structure requires successive solutions FEM operations, which further increases the computational cost.

Reducing the computational cost and removing the restriction of the amount of perturbation can be achieved by using the step-by-step eigenvalue perturbation method (Lu et al., 1993). Major benefit of the method is that only one FEM solution is required initially. Then, using this initial solution, new perturbed solutions can be obtained by using the step-by-step perturbation method more efficiently. Effectiveness of the step-by-step eigenvalue perturbation method for resonant cavity problems is shown by Gunel & Zoral, 2014 where the dielectric permittivity of the inner material of the cavity is perturbed. Initial FEM solutions were made with vector FEM, which provides spurious-free solutions. Thus, the quality of the perturbation solutions are only limited by the accuracy of the initial FEM solutions and the correct choice of the system parameters. Nonetheless, it is evident that the presence of any spurious modes also would have affected the results, if any had existed in the initial FEM solution.

The main goal of this study is to demonstrate the application of the step-by-step perturbation method along with the nodal FEM and investigating the effects of the spurious modes over the perturbation process. The problem will be modeled over a rectangular cavity that is filled with two different materials whose dielectric permittivities differ. The total amount of perturbation is divided into smaller steps in order to obtain a parametric history rather than eliminating the restriction about the amount of perturbation. Initially, cavity problem is solved by using FEM for a large interval of frequencies. Then, the size of the problem is significantly reduced by choosing the eigenvalues/eigenvectors which correspond to the lower order modes, at each step of the perturbation process. A software is created with Python language to implement the algorithm. Since the step-by-step perturbation method is heavily dependent on the initial FEM data, it was also necessary to create a nodal FEM routine since commercially available electromagnetic field solvers (e.g. Ansoft HFSS, CST Studio) don't provide any intermediary data about their processes.

1.2 Thesis Structure

The thesis is organized such that the theoretical analysis of resonant structures is given first, then the numerical results are presented.

Next chapter describes the analytical solutions of two types of cavities; one is uniformly filled cubic cavity where the dielectric permittivity of the inner material is constant everywhere and the other is partially filled cubic cavity which contains two materials with different permittivities. The expressions related with resonant frequencies are given for both structures. These expressions will be used extensively as reference to measure the performance of the numerical results.

Theoretical basis of nodal FEM and step-by-step perturbation technique are given in Chapter 3. First of all, FEM formulation is described in general, then it is shown that how the cavity problem is expressed as a generalized eigenvalue/eigenvector problem. The concept of spurious solution is explained shortly. After that, the classical perturbation method is given to introduce the concept of cavity perturbation and the limitation about the amount of variation is explained. Finally, the step-by-step perturbation method is given and its superiority over classical perturbation is mentioned.

Chapter 4 includes the numerical results for both FEM and the step-by-step perturbation routines, obtained by using the designed software. The numerical and the analytical solutions are compared for the cavity structures given in Chapter 2. Moreover, Ansoft HFSS is occasionally used to simulate the structures for further verification. Effects of two FEM parameters, mesh resolution and divergence coefficient, over the solutions are investigated. The step-by-step perturbation technique is tested with different parameters as well and several limitations about the process are pointed out. Finally, the effects of the spurious solutions over the step-by-step perturbation results are examined by using three error criteria.

CHAPTER TWO

ELECTROMAGNETIC RESONANCE PROBLEM

Electromagnetic cavity resonator is an empty enclosed object made from a good electrical conductor. The inner filling material is generally a lossless dielectric material that is chosen according to the requirements. They can find application in microwave circuits as resonance elements, similar to LC sections. Resonant cavities can provide excellent quality factor as the value may reach several thousands at resonant frequencies. Therefore, they are very desirable as an oscillator building block, especially at the frequencies where wavelength is sufficiently small. Frequency tuning is also possible with mechanical alterations, such as adding a screw that controls the position of an inner wall or inserting a material whose characteristics are different. An electromagnetic field can be excited with an inner probe or loop as well as coupling with a waveguide (Collin, 1992).



Figure 2.1 A cylindrical cavity

The resonance characteristics of a cavity resonator can be obtained by solving the Helmholtz wave equation (2.1) along with the necessary boundary conditions, for source-free case. Mathematical representation does not include any probe model or source term since they are redundant for analytical case.

$$\begin{aligned}\nabla^2 \mathbf{E} + \beta^2 \mathbf{E} &= 0 \\ \nabla^2 \mathbf{H} + \beta^2 \mathbf{H} &= 0\end{aligned}\tag{2.1}$$

where \mathbf{E} and \mathbf{H} are electric field intensity (V/m) and magnetic field intensity (A/m), respectively. The wavenumber, β , can be expressed as,

$$\beta^2 = \omega^2 \mu \epsilon\tag{2.2}$$

where ω is the angular frequency (rad/s), ϵ is the permittivity (F/m) and μ is the permeability (H/m) of the medium.

Existence of an analytical solution mostly depends on the geometry and the inner material properties (ϵ , μ). As a result, it is not always possible to find such solution. However, the cases where solutions exist, usually provide a reference point for evaluating the performance of approximate solution methods.

2.1 Analytical Solution For Cubic Cavity

Solving the Helmholtz wave equation for a cubic cavity is significantly easier and provides quicker, simpler results compared to different geometrical configurations. First of all, the wave equation is written in cartesian form, which is much simpler compared to cylindrical and spherical counterparts. Consequently, solutions are also simpler. Secondly, due to the symmetrical properties of the cube, resonances occur at the same frequencies (degenerate modes) for certain mode configurations, as long as the cavity is filled uniformly. This allows to tag and identify the resulting resonant frequencies produced by an approximate solution method (e.g FEM) very easily. For a partially filled cavity, resonant frequencies depend on the properties of the inner materials and the fill ratio, which increases the complexity of the equations. Nonetheless, analytical solutions still exist. Let us now investigate these two cavity structures.

2.1.1 Uniformly Filled Cubic Cavity

Analysis of resonant cavities is similar to waveguide solutions. Let us begin the analysis with transverse magnetic mode with respect to z direction (TM_z). Solution process of (2.1) can be simplified by introducing an auxiliary function, the magnetic vector potential \mathbf{A} , that satisfies the following identities (Balanis, 1989).

$$\begin{aligned}\mathbf{H} &= \frac{1}{\mu} \nabla \times \mathbf{A} \\ \mathbf{E} &= -j\omega\mathbf{A} - j\frac{1}{\omega\mu\epsilon} \nabla(\nabla \cdot \mathbf{A})\end{aligned}\tag{2.3}$$

leads to the following for TM_z case.

$$\begin{aligned}
H_x &= \frac{1}{\mu} \frac{\partial A_z}{\partial y} & E_x &= -j \frac{1}{\omega \epsilon \mu} \frac{\partial^2 A_z}{\partial x \partial z} \\
H_y &= -\frac{1}{\mu} \frac{\partial A_z}{\partial x} & E_y &= -j \frac{1}{\omega \epsilon \mu} \frac{\partial^2 A_z}{\partial y \partial z} \\
H_z &= 0 & E_z &= -j \frac{1}{\omega \epsilon \mu} \left(\frac{\partial^2}{\partial z^2} + \beta^2 \right) A_z
\end{aligned} \tag{2.4}$$

where $A_z(x, y, z)$ is the scalar component of \mathbf{A} towards z direction, which satisfies,

$$\begin{aligned}
\nabla^2 A_z(x, y, z) + \beta^2 A_z(x, y, z) &= 0 \\
\frac{\partial^2 A_z}{\partial x^2} + \frac{\partial^2 A_z}{\partial y^2} + \frac{\partial^2 A_z}{\partial z^2} + \beta^2 A_z &= 0
\end{aligned} \tag{2.5}$$

Solution of (2.5) can be obtained using separation of variables method such that,

$$\begin{aligned}
A_z(x, y, z) &= [A \cos(\beta_x x) + B \sin(\beta_x x)] [C \cos(\beta_y y) + D \sin(\beta_y y)] \\
&\quad \times [E \cos(\beta_z z) + F \sin(\beta_z z)] \\
\beta_x^2 + \beta_y^2 + \beta_z^2 &= \beta^2
\end{aligned} \tag{2.6}$$

A, B, C, D, E and F are the coefficients which must be found when (2.6) is substituted into (2.4) along with the necessary boundary conditions. Uniformly filled cavity has 6 boundaries that can be considered as perfect electrical conductors for convenience. The boundary conditions for electric and magnetic fields on a perfect electrical conducting surface are given as,

$$\begin{aligned}
\hat{\mathbf{n}} \times \mathbf{H} &= \mathbf{J}_s \\
\hat{\mathbf{n}} \times \mathbf{E} &= 0 \\
\hat{\mathbf{n}} \cdot \mathbf{H} &= 0 \\
\hat{\mathbf{n}} \cdot \mathbf{E} &= \frac{\rho_s}{\epsilon}
\end{aligned} \tag{2.7}$$

where \mathbf{J}_s is the surface current density (A/m²) and ρ_s is the surface charge density (C/m²). Since the region is source-free, right hand side of the first and the last equations in (2.7) equal to zero. Applying the boundary conditions, reduces (2.6) into the following form;

$$\begin{aligned}
A_z(x, y, z) &= K_{mnp} \sin(\beta_x x) \sin(\beta_y y) \cos(\beta_z z) \\
\beta_x &= \frac{m\pi}{a} & m = 1, 2, 3, \dots \\
\beta_y &= \frac{n\pi}{a} & n = 1, 2, 3, \dots \\
\beta_z &= \frac{p\pi}{a} & p = 0, 1, 2, \dots \\
\beta = \omega \sqrt{\mu\epsilon} &= \sqrt{\left(\frac{m\pi}{a}\right)^2 + \left(\frac{n\pi}{a}\right)^2 + \left(\frac{p\pi}{a}\right)^2}
\end{aligned} \tag{2.8}$$

where a is the side length of the cube. m, n, p indices represent the mode configurations and can take the values given in (2.8). The resonant frequency for any numerical configuration can be calculated from (2.8) by substituting the permittivity and the permeability values at the left hand side of the equation. The mode having the lowest resonant frequency is called as the dominant mode.

A similar procedure can be applied for finding TE mode solutions by means of the electric vector potential \mathbf{F} .

$$\begin{aligned}
F_z(x, y, z) &= [A \cos(\beta_x x) + B \sin(\beta_x x)] [C \cos(\beta_y y) + D \sin(\beta_y y)] \\
&\quad \times [E \cos(\beta_z z) + F \sin(\beta_z z)]
\end{aligned} \tag{2.9}$$

If the boundary conditions are applied,

$$\begin{aligned}
F_z(x, y, z) &= K_{mnp} \cos(\beta_x x) \cos(\beta_y y) \sin(\beta_z z) \\
\beta_x &= \frac{m\pi}{a} & m = 0, 1, 2, \dots \\
\beta_y &= \frac{n\pi}{a} & n = 0, 1, 2, \dots \\
\beta_z &= \frac{p\pi}{a} & p = 1, 2, 3, \dots \\
m &= n \neq 0
\end{aligned} \tag{2.10}$$

The resonant frequency expression is found as the same as given in (2.8), but the numerical configurations differ for m, n, p , as it is seen in (2.10). It can be noticed that cubic cavity have three dominant modes (TM_{110} , TE_{011} , TE_{101}) which are also degenerate (have the same resonant frequency). Such degenerate modes occur at many other frequencies due to the symmetry. The ratio between the resonant frequency of TM_{110} , TE_{011} , TE_{101} and following 11 modes, including the TE cases, for a cubic cavity is summarized in Table 2.1.

Table 2.1 Resonant frequency comparison for cubic cavity

	TE ₁₀₁	TE ₀₁₁	TM ₁₁₀	TE ₁₁₁	TM ₁₁₁	TE ₁₀₂	TE ₂₀₁
$\frac{f(\cdot)}{f(\text{TM}_{110})}$	1			1.22		1.58	
	TE ₀₂₁	TE ₀₁₂	TM ₂₁₀	TM ₁₂₀	TE ₁₁₂	TM ₁₁₂	TM ₁₃₀
	1.58				1.73		2.23

2.1.2 Partially Filled Cubic Cavity

A partially filled cavity generally contains two materials whose permittivities or permeabilities or both differ from each other. The reason for such modification is tuning the resonance frequency without changing the dimensions of the cavity. Despite that the cavities whose one dimension can be varied mechanically are common, tuning intervals are rather limited compared to the material perturbation.

For our practical purposes, let us consider a cubic cavity containing two materials having the same permeability but different permittivities as shown in Figure 2.2. For this specific material configuration, where the dielectric constant varies along the z -direction, none of the TM _{x} , TM _{y} , TE _{x} or TE _{y} solutions satisfy the boundary conditions individually (Harrington, 2001). Therefore, TM _{z} and TE _{z} cases must be investigated.

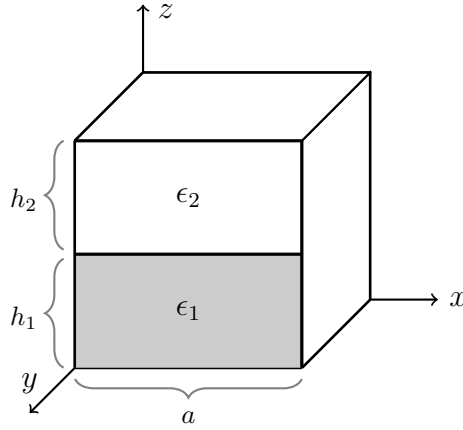


Figure 2.2 Partially filled cavity illustration

Let us define two scalar magnetic potential functions for the regions filled with ϵ_1 and ϵ_2 .

$$\begin{aligned}
A_z^{(1)}(x, y, 0 \leq z \leq h_1) &= [A^{(1)} \cos(\beta_x^{(1)} x) + B^{(1)} \sin(\beta_x^{(1)} x)] [C^{(1)} \cos(\beta_y^{(1)} y) + \\
&\quad D^{(1)} \sin(\beta_y^{(1)} y)] [E^{(1)} \cos(\beta_z^{(1)} z) + F^{(1)} \sin(\beta_z^{(1)} z)] \\
A_z^{(2)}(x, y, h_1 \leq z \leq a) &= [A^{(2)} \cos(\beta_x^{(2)} x) + B^{(2)} \sin(\beta_x^{(2)} x)] [C^{(2)} \cos(\beta_y^{(2)} y) + \\
&\quad D^{(2)} \sin(\beta_y^{(2)} y)] [E^{(2)} \cos(\beta_z^{(2)} (a - z)) + F^{(2)} \sin(\beta_z^{(2)} (a - z))]
\end{aligned} \tag{2.11}$$

The field expressions can be found using (2.4) in the same way. Applying the boundary conditions for magnetic field at $x = 0$, $x = a$, $y = 0$ and $y = a$ planes yields to the following.

$$\begin{aligned}
H_x^{(1)}(x = (0, a), 0 \leq y \leq a, 0 \leq z \leq h_1) &= 0 \\
H_y^{(1)}(0 \leq x \leq a, y = (0, a), 0 \leq z \leq h_1) &= 0 \\
H_x^{(2)}(x = (0, a), 0 \leq y \leq a, h_1 \leq z \leq a) &= 0 \\
H_y^{(2)}(0 \leq x \leq a, y = (0, a), h_1 \leq z \leq a) &= 0
\end{aligned} \tag{2.12}$$

which leads to,

$$\begin{aligned}
A^{(1)} &= C^{(1)} = A^{(2)} = C^{(2)} = 0 \\
A_z^{(1)} &= K_{mn}^{(1)} \sin(\beta_x^{(1)} x) \sin(\beta_y^{(1)} y) [E^{(1)} \cos(\beta_z^{(1)} z) + F^{(1)} \sin(\beta_z^{(1)} z)] \\
A_z^{(2)} &= K_{mn}^{(2)} \sin(\beta_x^{(2)} x) \sin(\beta_y^{(2)} y) [E^{(2)} \cos(\beta_z^{(2)} (a - z)) + F^{(2)} \sin(\beta_z^{(2)} (a - z))]
\end{aligned} \tag{2.13}$$

with,

$$\begin{aligned}
\beta_x^{(1)} &= \frac{m^{(1)} \pi}{a}, \quad \beta_x^{(2)} = \frac{m^{(2)} \pi}{a}, \quad \beta_y^{(1)} = \frac{n^{(1)} \pi}{a}, \quad \beta_y^{(2)} = \frac{n^{(2)} \pi}{a} \\
m^{(1)} &= 0, 1, 2, \dots \quad n^{(1)} = 1, 2, \dots \quad m^{(2)} = 0, 1, 2, \dots \quad n^{(2)} = 1, 2, \dots
\end{aligned} \tag{2.14}$$

The potential functions can be further simplified using boundary conditions for electric fields at $z = 0$ and $z = a$ planes.

$$\begin{aligned}
E_x^{(1)}(0 \leq x \leq a, 0 \leq y \leq a, z = 0) &= E_y^{(1)}(0 \leq x \leq a, 0 \leq y \leq a, z = 0) = 0 \\
E_x^{(2)}(0 \leq x \leq a, 0 \leq y \leq a, z = a) &= E_y^{(2)}(0 \leq x \leq a, 0 \leq y \leq a, z = a) = 0 \\
F^{(1)} &= F^{(2)} = 0 \\
A_z^{(1)} &= K_{mn}^{(1)} \sin(\beta_x^{(1)} x) \sin(\beta_y^{(1)} y) \cos(\beta_z^{(1)} z) \\
A_z^{(2)} &= K_{mn}^{(2)} \sin(\beta_x^{(2)} x) \sin(\beta_y^{(2)} y) \cos(\beta_z^{(2)} (a - z))
\end{aligned} \tag{2.15}$$

In order to find a proper expression which relates $A_z^{(1)}$ and $A_z^{(2)}$, dielectric interface must be examined. The boundary conditions for dielectric interface are given as,

$$\begin{aligned}\hat{\mathbf{n}} \times (\mathbf{E}^{(2)} - \mathbf{E}^{(1)}) &= 0 \\ \hat{\mathbf{n}} \times (\mathbf{H}^{(2)} - \mathbf{H}^{(1)}) &= \mathbf{J}_s\end{aligned}\quad (2.16)$$

Since the cavity doesn't contain any source, right hand side of the boundary formula for magnetic fields is equal to zero. Thus, tangential components of the electric and magnetic fields across the boundary are continuous.

$$H_x^{(1)} = H_x^{(2)}, \quad H_y^{(1)} = H_y^{(2)}, \quad E_x^{(1)} = E_x^{(2)}, \quad E_y^{(1)} = E_y^{(2)} \quad \text{at } z = h_1 \quad (2.17)$$

Evaluating $H_x^{(1)}$ and $H_x^{(2)}$ at dielectric interface results,

$$\begin{aligned}H_x^{(1)} &= \frac{\beta_y^{(1)}}{\mu} K_{mn}^{(1)} \sin(\beta_x^{(1)} x) \cos(\beta_y^{(1)} y) \cos(\beta_z^{(1)} h_1) \\ H_x^{(2)} &= \frac{\beta_y^{(2)}}{\mu} K_{mn}^{(2)} \sin(\beta_x^{(2)} x) \cos(\beta_y^{(2)} y) \cos(\beta_z^{(2)} (a - h_1))\end{aligned}\quad (2.18)$$

From (2.18) it is evident that $\beta_x^{(1)} = \beta_x^{(2)}$ and $\beta_y^{(1)} = \beta_y^{(2)}$. Hence, the expressions are reduced into the following form.

$$\begin{aligned}A_z^{(1)} &= K_{mn}^{(1)} \sin(\beta_x x) \sin(\beta_y y) \cos(\beta_z^{(1)} z) \\ A_z^{(2)} &= K_{mn}^{(2)} \sin(\beta_x x) \sin(\beta_y y) \cos(\beta_z^{(2)} (a - z)) \\ \beta_x &= \frac{m\pi}{a} \quad m = 0, 1, 2, \dots, \quad \beta_y = \frac{n\pi}{a} \quad n = 1, 2, \dots \\ \beta^{(1)} &= \sqrt{(\beta_x)^2 + (\beta_y)^2 + (\beta_z^{(1)})^2} = \omega \sqrt{\mu \epsilon_1} \\ \beta^{(2)} &= \sqrt{(\beta_x)^2 + (\beta_y)^2 + (\beta_z^{(2)})^2} = \omega \sqrt{\mu \epsilon_2}\end{aligned}\quad (2.19)$$

Continuity of the magnetic field expressions given in (2.18) results,

$$K_{mn}^{(1)} \cos(\beta_z^{(1)} h_1) = K_{mn}^{(2)} \cos(\beta_z^{(2)} (a - h_1)) \quad (2.20)$$

Similarly, continuity of the electric fields across the boundary results,

$$\frac{\beta_z^{(1)}}{\epsilon_1} K_{mn}^{(1)} \sin(\beta_z^{(1)} h_1) = -\frac{\beta_z^{(2)}}{\epsilon_2} K_{mn}^{(2)} \sin(\beta_z^{(2)} (a - h_1)) \quad (2.21)$$

Dividing the (2.21) by (2.20) gives the characteristic equation;

$$\frac{\beta_z^{(1)}}{\epsilon_1} \tan(\beta_z^{(1)} h_1) + \frac{\beta_z^{(2)}}{\epsilon_2} \tan(\beta_z^{(2)} (a - h_1)) = 0 \quad (2.22)$$

where,

$$\begin{aligned} \beta_z^{(1)}(\omega) &= \sqrt{\omega^2 \mu \epsilon_1 - \left(\frac{m\pi}{a}\right)^2 - \left(\frac{n\pi}{a}\right)^2} \\ \beta_z^{(2)}(\omega) &= \sqrt{\omega^2 \mu \epsilon_2 - \left(\frac{m\pi}{a}\right)^2 - \left(\frac{n\pi}{a}\right)^2} \end{aligned} \quad (2.23)$$

A similar approach can be used to obtain the characteristic equation for TE case, which results,

$$\frac{\beta_z^{(1)}}{\mu} \cot(\beta_z^{(1)} h_1) + \frac{\beta_z^{(2)}}{\mu} \cot(\beta_z^{(2)} (a - h_1)) = 0 \quad (2.24)$$

From (2.23) and (2.24), it is inferred that the resonant frequency is obtained by finding the roots of the trigonometric equation for a particular choice of m and n numbers. Since the expressions cannot be simplified any further and there is not a structured method to solve the equations, numerical methods (e.g Newton-Raphson method) or graphical evaluations are required to find the solutions. Nevertheless, it is possible to make rough estimations using perturbational techniques prior to solving characteristic equation. In general, it can be shown that the resonant frequency of a partially filled cavity for a particular mode, lie between the resonant frequencies of uniform cavities filled with materials having dielectric constants ϵ_1 and ϵ_2 , for the same particular mode (Balanis, 1989; Collin, 1990).

$$f(\epsilon_2) < f(\epsilon_{\text{partial}}) < f(\epsilon_1) \quad \text{for} \quad \epsilon_2 > \epsilon_1 \quad (2.25)$$

Periodicity of the functions implies that infinite number of solutions for a particular m, n pair. However, it is generally sufficient to investigate only two roots with lowest frequencies, for most practical applications. Although there is no proper numbering convention like in uniform cavity case, a number p , which increases with respect to the frequency for a particular m and n , can be defined (Harrington, 2001). Resulting waveforms don't have a regular pattern like uniform cavity resonance. Fields tend to be concentrated in the region having higher permittivity and/or permeability. Both the electric and the magnetic fields inside the cavity have z components for certain modes, which are called *hybrid* modes.

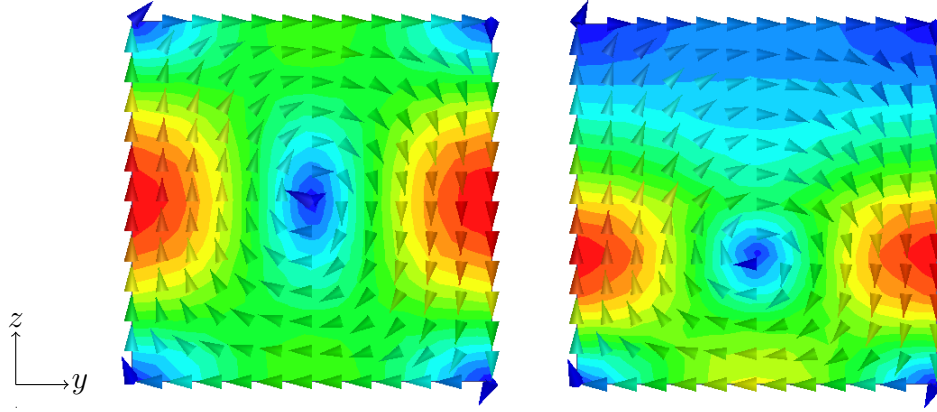


Figure 2.3 Magnetic field illustrations of an empty (left) and a partially filled cavity (right)

2.2 Cavity Problems without Analytical Solutions

As stated in previous section, filling a cavity partially with a material is useful for tuning the resonance frequency without changing the dimensions. This may not be always practical though, due to several limitations. In order to fill the cavity with another dielectric up to a certain volume, at least one bulk material has to be shaped to satisfy the dimensions, assuming that the second dielectric is vacuum or air. However, shaping may not always be possible, depending on material and its dimensions and even if it is, manufacturing process might introduce some defects which cause erroneous operation. As a result, the materials which are used for tuning the cavity, may have geometries and dimensions different than the cavity itself, like shown in Figure 2.4.

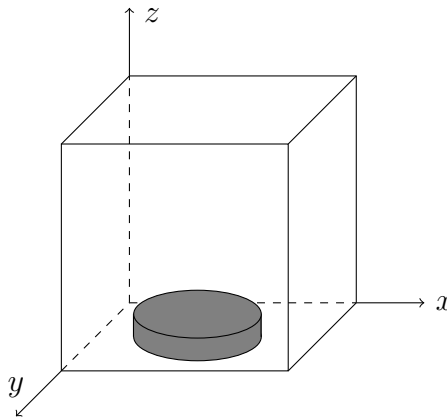


Figure 2.4 An empty rectangular cavity with a pill-shaped dielectric material

Major problem for this case and many similar others, is the lack of the analytical solutions. Although there are approximations for common cavity and dielectric configurations in order to find resonance frequency (Harrington, 2001), they can't

be generalized for every possible situation. For this reason, verification of these structures are made using numerical methods. There are several numerical methods for solving electromagnetic problems. Finite Element Method (FEM), Method of Moments (MoM), Finite Difference Time Domain (FDTD) are some of the most common techniques used today. Analysis of the cavity resonance problem by means of FEM yields an eigenvalue problem, which, in result, brings the resonant frequency information we want to find at first place.

CHAPTER THREE

FINITE ELEMENT METHOD AND STEP-BY-STEP EIGENVALUE PERTURBATION FOR CAVITY PROBLEM

3.1 Finite Element Method

Finite Element Method (FEM) is a numerical analysis tool for solving boundary value problems defined by differential equations for a given domain. It is widely used to solve many physical problems from different areas like electromagnetics, thermodynamics, structural mechanics, fluid dynamics. Main motivation for using FEM is to find approximate solutions to the problems that can't be solved analytically. Solution is obtained by dividing the entire domain into smaller pieces (discretization), then solving a set of equations represented in matrix form (Logan, 2011).

Eigenvalue problems in FEM are special type of problems where the differential equation and the boundary conditions are homogeneous, meaning no source exists in the system. Resulting algebraic system can be expressed in the following form;

$$\mathbf{A}\phi = \lambda\mathbf{B}\phi \quad (3.1)$$

where λ is an eigenvalue and ϕ is the eigenvector corresponding to λ . Typical applications of the eigenvalue problem formulation for electromagnetics are waveguide and cavity problems. Let us now review the general formulation of FEM, then its application to resonant cavities as an eigenvalue problem.

3.1.1 General Finite Element Method Formulation

Mathematical foundations of FEM is based on classical methods for solving boundary value problems. The two well known and widely used of these methods are Galerkin method and Ritz' variational method. Both formulations result the same system of equations. Ritz' formulation can be summarized briefly in the following form.

Suppose that a boundary value problem is defined by a governing differential equation in domain Ω , along with the boundary conditions on the boundary Γ .

$$\mathcal{L}\tilde{\phi} = f \quad (3.2)$$

where \mathcal{L} is the differential operator, f is the excitation and $\tilde{\phi}$ is the unknown term. Let us assume the problem is real valued and \mathcal{L} is a self-adjoint operator. Then, the solution of (3.2) can be found by minimizing the following functional with respect to $\bar{\phi}$.

$$F(\bar{\phi}) = \frac{1}{2} \langle \mathcal{L}\bar{\phi}, \bar{\phi} \rangle - \langle \bar{\phi}, f \rangle \quad (3.3)$$

where $\bar{\phi}$ is the trial function. It should be noted that the term $\bar{\phi}$ represents the field expressions (electric field, magnetic field) for an electromagnetic problem. There are generally two types of boundary conditions in electromagnetic problems. First one is Dirichlet boundary condition which defines $\bar{\phi}$ at the boundaries and the second condition is Neumann condition which determines the value of the derivative of $\bar{\phi}$ at boundaries. Implementation of Dirichlet conditions require explicit definition while Neumann conditions are generally satisfied within the solution process automatically (Jin, 2002).

Finite element analysis requires the solution domain to be discretized and divided into smaller subdomains, which are also called as elements and they can be denoted by Ω^e for $e = 1, 2, 3, \dots, M$ where M is the number of elements. For a three dimensional geometry, these elements may have various shapes like brick, prism, tetrahedra.

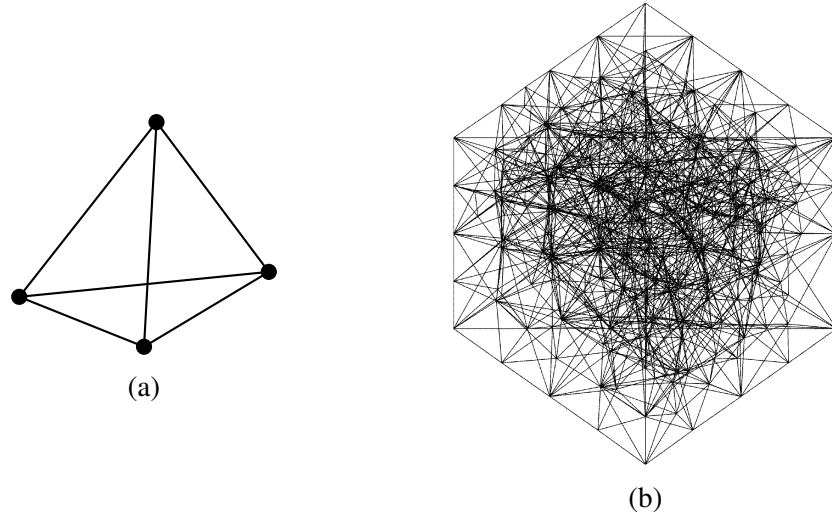


Figure 3.1 (a) A tetrahedral element (b) Discretization of a cube with tetrahedral elements (Wilson, 1984)

The solution is obtained as a vector which represents the values of the unknown term at node points. This type of modeling is called as nodal FEM. Values inside the elements at arbitrary points are obtained by means of interpolation functions. Type of the interpolation function is generally a trade-off between complexity and accuracy. However, as long as the discretization is sufficiently refined, linear functions

are favorable due their simplicity. For a mesh which is formed by tetrahedral elements, unknown solution constituted with linear interpolation can be written in the following form for a single element.

$$\bar{\phi}^e = \sum_{i=1}^4 N_i^e \phi_i^e = (N^e)^T (\phi^e) \quad (3.4)$$

where N_i^e is the interpolation functions and ϕ_i is the value which must be found at node i . Elemental functions contributes to the major problem in the following form;

$$F(\bar{\phi}) = \sum_{e=1}^M F^e(\bar{\phi}^e) \quad (3.5)$$

where

$$F^e(\bar{\phi}^e) = \frac{1}{2} \int_{\Omega^e} \bar{\phi}^e \mathcal{L} \bar{\phi}^e d\Omega - \int_{\Omega^e} f \bar{\phi}^e d\Omega \quad (3.6)$$

Substituting (3.4) into (3.6),

$$\begin{aligned} F^e &= \frac{1}{2} (\phi^e)^T (K^e) (\phi^e) - (\phi^e)^T (b^e) \\ K_{ij}^e &= \int_{\Omega^e} N_i^e \mathcal{L} N_j^e d\Omega \\ b_i^e &= \int_{\Omega^e} f N_i^e d\Omega \end{aligned} \quad (3.7)$$

where ϕ^e, b^e are 4×1 column vectors, K^e is 4×4 matrix. Returning back to original formulation given in (3.5) with a global node numbering convention gives,

$$\begin{aligned} F &= \frac{1}{2} (\phi)^T (K) (\phi) - (\phi)^T (b) \\ K &= \sum_{e=1}^M K^e \\ b &= \sum_{e=1}^M b^e \end{aligned} \quad (3.8)$$

where K is $n \times n$ matrix known as the *stiffness matrix* and b is a $n \times 1$ vector. n is the total number of the nodes obtained by the discretization of the entire domain. The minimization of the functional F given in (3.8) results,

$$\mathbf{K}\phi = \mathbf{b} \quad (3.9)$$

The system given in (3.9) can be solved right after the boundary conditions are applied. Imposition of Dirichlet condition in this matrix system is very simple as it can be accomplished by setting the entire matrix line and column concerning the boundary node to zero, except the diagonal element, which should be set to 1. On the other hand, implementation of Neumann condition is more complicated as it requires the alteration of functional. However, as long as the interpolation functions don't violate continuity, Neumann conditions don't have to be enforced explicitly. It must be noted that though, this approach will cause spurious solutions since the conditions cannot be satisfied completely due to discretization (Gunel & Zoral, 2012; Rahman et al., 1991).

For the case where no excitation exists in the given system, right-hand side of (3.9) reduces to zero. If the stiffness matrix can be decomposed in the following form,

$$\mathbf{K} = \mathbf{A} - \lambda\mathbf{B} \quad (3.10)$$

then (3.9) becomes,

$$\mathbf{A}\phi = \lambda\mathbf{B}\phi \quad (3.11)$$

which is in the form of an eigenvalue problem. Let us now apply FEM formulation to a rectangular cavity.

3.1.2 Finite Element Formulation For Rectangular Cavity

The analysis of a rectangular cavity requires either the electric or magnetic fields to be treated, which are both vector quantities. Therefore, modifications are required in the formulation of the problem. It should be noted that using magnetic field formulation provides a significant advantage for dielectric cavity problem since the magnetic field doesn't have any discontinuities in the structure (Rahman et al., 1991). Hence, the magnetic field formulation will be used for the problem.

For the time harmonic case, magnetic field expression inside of a rectangular cavity can be obtained by solving,

$$\nabla \times \left(\frac{1}{\epsilon_r} \nabla \times \mathbf{H} \right) - k_0^2 \mu_r \mathbf{H} = 0 \quad (3.12)$$

with the following boundary condition at perfect electrical conductor surfaces.

$$\hat{\mathbf{n}} \cdot \mathbf{H} = 0 \quad (3.13)$$

The functional which corresponds to this boundary value problem can be written as,

$$F(\mathbf{H}) = \frac{1}{2} \iiint_V \left[\frac{1}{\epsilon_r} (\nabla \times \mathbf{H}) \cdot (\nabla \times \mathbf{H}) - k_0^2 \mu_r \mathbf{H} \cdot \mathbf{H} \right] dV \quad (3.14)$$

Simplifying the expression in terms of H_x, H_y, H_z results,

$$F = \frac{1}{2} \iiint_V \frac{1}{\epsilon_r} \left[\left(\frac{\partial H_z}{\partial y} - \frac{\partial H_y}{\partial z} \right)^2 + \left(\frac{\partial H_x}{\partial z} - \frac{\partial H_z}{\partial x} \right)^2 + \left(\frac{\partial H_y}{\partial x} - \frac{\partial H_x}{\partial y} \right)^2 \right. \\ \left. - k_0^2 \mu_r \epsilon_r (H_x^2 + H_y^2 + H_z^2) \right] dV \quad (3.15)$$

Due to the dependency between H_x, H_y, H_z , resulting system of equations contains coupling terms, which are also in matrix form.

$$\begin{pmatrix} K_{xx} & K_{xy} & K_{xz} \\ K_{yx} & K_{yy} & K_{yz} \\ K_{zx} & K_{zy} & K_{zz} \end{pmatrix} \begin{pmatrix} H_x \\ H_y \\ H_z \end{pmatrix} = 0 \quad (3.16)$$

Rank of the matrix is $3n$, where n is the total number of the nodes. Individual parts of this matrix can be expressed as,

$$K_{xx} = \sum_{e=1}^M \frac{1}{\epsilon_r} \iiint_{V^e} \left[\left(\frac{\partial N^e}{\partial y} \right) \left(\frac{\partial N^e}{\partial y} \right)^T + \left(\frac{\partial N^e}{\partial z} \right) \left(\frac{\partial N^e}{\partial z} \right)^T \right. \\ \left. - k_0^2 \mu_r \epsilon_r (N^e)(N^e)^T \right] dV$$

$$K_{yy} = \sum_{e=1}^M \frac{1}{\epsilon_r} \iiint_{V^e} \left[\left(\frac{\partial N^e}{\partial z} \right) \left(\frac{\partial N^e}{\partial z} \right)^T + \left(\frac{\partial N^e}{\partial x} \right) \left(\frac{\partial N^e}{\partial x} \right)^T \right. \\ \left. - k_0^2 \mu_r \epsilon_r (N^e)(N^e)^T \right] dV$$

$$K_{zz} = \sum_{e=1}^M \frac{1}{\epsilon_r} \iiint_{V^e} \left[\left(\frac{\partial N^e}{\partial x} \right) \left(\frac{\partial N^e}{\partial x} \right)^T + \left(\frac{\partial N^e}{\partial y} \right) \left(\frac{\partial N^e}{\partial y} \right)^T - k_0^2 \mu_r \epsilon_r (N^e)(N^e)^T \right] dV \quad (3.17)$$

$$K_{pq} = \sum_{e=1}^M \frac{1}{\epsilon_r} \iiint_{V^e} \left[\left(\frac{\partial N^e}{\partial p} \right) \left(\frac{\partial N^e}{\partial q} \right)^T \right] dV \quad p, q = x, y, z \quad p \neq q$$

If the following definitions are made,

$$\begin{aligned} B_{xx} &= \sum_{e=1}^M \iiint_{V^e} (N^e)(N^e)^T dV \\ B_{yy} &= \sum_{e=1}^M \iiint_{V^e} (N^e)(N^e)^T dV \\ B_{zz} &= \sum_{e=1}^M \iiint_{V^e} (N^e)(N^e)^T dV \end{aligned} \quad (3.18)$$

$$\begin{aligned} A_{xx} &= K_{xx} - k_0^2 \mu_r B_{xx} \\ A_{yy} &= K_{yy} - k_0^2 \mu_r B_{yy} \\ A_{zz} &= K_{zz} - k_0^2 \mu_r B_{zz} \\ A_{pq} &= K_{pq} \quad p, q = x, y, z \quad p \neq q \end{aligned}$$

the system of equations can be separated in the following form,

$$\begin{pmatrix} A_{xx} & A_{xy} & A_{xz} \\ A_{yx} & A_{yy} & A_{yz} \\ A_{zx} & A_{zy} & A_{zz} \end{pmatrix} \begin{pmatrix} H_x \\ H_y \\ H_z \end{pmatrix} = k_0^2 \mu_r \begin{pmatrix} B_{xx} & 0 & 0 \\ 0 & B_{yy} & 0 \\ 0 & 0 & B_{zz} \end{pmatrix} \begin{pmatrix} H_x \\ H_y \\ H_z \end{pmatrix} \quad (3.19)$$

which is an eigenvalue-eigenvector problem. There are various algorithms in literature for solving (3.19). Symmetry and sparsity properties of the matrices allow the computations to be more efficient (Bai et al., 2000). The accuracy of the resulting eigenvalues and eigenvectors mostly depends on the number of the nodes, which affects the solution time and memory requirements exponentially.

3.1.3 Spurious Modes

One of the most intriguing concepts in finite element analysis is the existence of nonphysical (spurious) solutions. There are many studies which address this issue for waveguides particularly (Mabaya et al., 1981; Ise et al., 1990; Sun et al., 1995), as well as different methods to deal with. Reasons for this problem can be given as the representation of the differential equation in weak form and discretization of the domain, which is mentioned previously.

There are various methods to deal with spurious solutions. One approach is based on selecting continuous interpolation functions whose derivatives are also continuous, namely, C^1 functions. This approach hasn't become popular due to the difficulties of implementation. Another method which is widely used today is using edge based elements instead of nodal ones (Cendes, 1991). This method is known as *Vector FEM* and requires more complicated formulations compared to nodal FEM. However, this approach is out of the scope of this study, therefore an alternative way, namely, penalty term method is investigated. Penalty term method relies on adding a divergence term to the functional, which is based on the fact that spurious solutions don't satisfy the following condition.

$$\nabla \cdot \mathbf{H} = 0 \quad (3.20)$$

Hence, the functional is modified in the following form.

$$F(\mathbf{H}) = \frac{1}{2} \iiint_V \left[\frac{1}{\epsilon_r} (\nabla \times \mathbf{H}) \cdot (\nabla \times \mathbf{H}) + \frac{s}{\mu_r^2 \epsilon_r} [\nabla \cdot (\mu_r \mathbf{H})]^2 - k_0^2 \mu_r \mathbf{H} \cdot \mathbf{H} \right] dV \quad (3.21)$$

where s is the penalty coefficient. It should be noted that introducing the penalty term doesn't violate symmetry or sparsity and don't increase the size of the problem. Although spurious solutions are not completely avoided, eigenvalues which correspond to spurious solutions are mostly shifted towards higher frequencies. This is a significant advantage for cavity problem as the modes of interest generally cover lower frequencies.

3.2 Step-By-Step Eigenvalue Perturbation Technique For Resonant Cavity Structures

Certain parameters of electromagnetic resonant structures may be slightly varied for tuning, optimization or sensitivity analysis. In literature, this problem has been

referred as perturbation problem. Perturbation of these structures with respect to a geometrical or a material parameter results in generalized eigenvalue-eigenvector perturbation problem. If the perturbation is sufficiently small, the well-known classical perturbation theory can be used to calculate resonant frequencies approximately (Van Bladel, 2007). On the other hand, if the perturbation is relatively large, the perturbation may be divided into smaller steps and the problem can be solved iteratively. Commercial FEM softwares handle this problem by solving the eigenvalue-eigenvector problem for each step successively, but this is time consuming since the number of unknowns may easily exceed several thousands and the computational costs of the algorithms for solving such problem are no less than $\mathcal{O}(n^2)$ (Bai et al., 2000). However, it is possible to examine the system for parameter variations by means of the step-by-step eigenvalue perturbation technique (Gunel & Zoral, 2014; Lu et al., 1993). In this section, the classical eigenvalue perturbation technique will be reviewed briefly, then the step-by-step perturbation method for a partially filled cavity will be explained.

3.2.1 Classical Eigenvalue Perturbation Method

Let us consider the generalized eigenvalue problem obtained by finite element formulation given in the following form;

$$\mathbf{A}_0 \phi_{0,i} = \lambda_{0,i} \mathbf{B}_0 \phi_{0,i} \quad (3.22)$$

where, $\mathbf{A}_0, \mathbf{B}_0 \in \mathbb{R}^{N \times N}$ and symmetric Hermitian matrices, $\phi_0 \in \mathbb{R}^N, i = 1, 2, \dots, N$

Applying small perturbations to matrices \mathbf{A}_0 and \mathbf{B}_0 such that $\|\Delta \mathbf{A}\| \ll \|\mathbf{A}_0\|$, $\|\Delta \mathbf{B}\| \ll \|\mathbf{B}_0\|$ results a new eigenvalue problem in the following form;

$$\mathbf{A} \phi_i = \lambda_i \mathbf{B} \phi_i \quad (3.23)$$

where,

$$\begin{aligned} \mathbf{A} &= \mathbf{A}_0 + \Delta \mathbf{A} \\ \mathbf{B} &= \mathbf{B}_0 + \Delta \mathbf{B} \\ \phi_i &= \phi_{0,i} + \Delta \phi_i \\ \lambda_i &= \lambda_{0,i} + \Delta \lambda_i \end{aligned} \quad (3.24)$$

then the perturbed eigenvalues-eigenvectors can be obtained by (Stewart & Sun, 1990),

$$\begin{aligned}\lambda_i &= \frac{(\phi_{0,i})^T \mathbf{A}(\phi_{0,i})}{(\phi_{0,i})^T \mathbf{B}(\phi_{0,i})} \\ \phi_i &= \phi_{0,i} + \sum_{j, j \neq i} \frac{(\phi_{0,j})^T (\mathbf{A} - \lambda_i \mathbf{B})(\phi_{0,i})}{\lambda_i - \lambda_{0,j}} \phi_{0,j}\end{aligned}\tag{3.25}$$

In the case of a permittivity perturbation of the resonant cavity where the eigenvalue problem is modeled by (3.21), $\Delta \mathbf{B} = 0$, $\mathbf{B} = \mathbf{B}_0$. It is evident that $\|\Delta \mathbf{A}\| \ll \|\mathbf{A}_0\|$ may not always be satisfied as the typical values for relative permittivity may vary between 1-100. Overcoming this problem is possible by dividing the perturbation into smaller steps and solving it iteratively.

3.2.2 Step-by-Step Eigenvalue Perturbation Method

Suppose that (3.22) is the FEM formulation obtained from (3.21) for the partially filled cavity illustrated in Figure 2.2 where $\epsilon_1 = \epsilon_0 \epsilon_{r1}$, $\epsilon_2 = \epsilon_0 \epsilon_{r2}$. If the permittivity of the material in the region 1 is varied from ϵ_1 to ϵ_{final} in K steps, the problem can be expressed in the following form;

$$[\mathbf{A}^{(k)} + \Delta f^{(k)} \Delta \mathbf{A}] \phi_i^{(k+1)} = \lambda_i^{(k+1)} \mathbf{B}^{(k)} \phi_i^{(k+1)}\tag{3.26}$$

where,

$$\begin{aligned}\epsilon^{(k)} - \epsilon^{(k-1)} &= \Delta \epsilon = \frac{\epsilon_{final} - \epsilon_1}{K} \\ f : \mathbb{R}^+ &\rightarrow \mathbb{R}^+ \quad f(\epsilon) = \frac{1}{\epsilon} \\ \Delta f^{(k)} &= f(\epsilon^{(k)}) - f(\epsilon^{(k-1)}) \\ \mathbf{A}^{(0)} &= \mathbf{A}_0 \quad \mathbf{B}^{(0)} = \mathbf{B}_0 \\ \lambda_i^{(0)} &= \lambda_{0,i} \quad \phi_i^{(0)} = \phi_{0,i}\end{aligned}\tag{3.27}$$

and k denotes the iteration step (Günel & Zoral, 2010).

It is unnecessary to find all the eigenvalues for a resonant cavity problem since the modes of interest are generally a few having the smallest frequencies. Suppose that FEM matrices are $N \times N$ and the number of modes which are interested is N_0 where $N > N_0$. If the original eigenvalue problem is written in the matrix form such that,

$$[\mathbf{A}^{(k)} + \Delta f^{(k)} \Delta \mathbf{A}] \Phi^{(k+1)} = \mathbf{B}^{(k)} \Phi^{(k+1)} \Lambda^{(k+1)}\tag{3.28}$$

where,

$$\begin{aligned}\Phi^{(k)} &= [\phi_1^{(k)} \ \phi_2^{(k)} \ \dots \ \phi_N^{(k)}] \\ \Lambda^{(k)} &= \text{diag} \left(\lambda_1^{(k)} \ \lambda_2^{(k)} \ \dots \ \lambda_N^{(k)} \right)\end{aligned}\tag{3.29}$$

Since $\mathbf{A}^{(k)}$, $\mathbf{B}^{(k)}$ are real symmetric matrices and $\Phi^{(k)}$ is the matrix whose column elements (eigenvectors) create an orthonormal basis,

$$\begin{aligned}\Lambda^{(k)} &= (\Phi^{(k)})^T \mathbf{A}^{(k)} (\Phi^{(k)}) \\ \mathbf{I} &= (\Phi^{(k)})^T \mathbf{B}^{(k)} (\Phi^{(k)})\end{aligned}\tag{3.30}$$

where \mathbf{I} is the identity matrix. If the following definitions are made,

$$\begin{aligned}\Phi^{(k+1)} &= \Phi^{(k)} \mathbf{Y}_{N_0 \times N_0}^{(k)} \\ \Phi^{(k)} &= [\phi_1^{(k)} \ \phi_2^{(k)} \ \dots \ \phi_{N_0}^{(k)}]\end{aligned}\tag{3.31}$$

then (3.28) can be written in the following form

$$\left[\mathbf{A}_{N_0 \times N_0}^{(k)} + \Delta f^{(k)} \Delta \mathbf{A} \right] \Phi^{(k)} \mathbf{Y}^{(k)} = \mathbf{B}^{(k)} \Phi^{(k)} \mathbf{Y}^{(k)} \Lambda^{(k+1)}\tag{3.32}$$

If the expression is multiplied by $(\Phi^{(k)})^T$ from both sides,

$$\left[\Lambda_{N_0 \times N_0}^{(k)} + \Delta f^{(k)} (\Phi^{(k)})^T \Delta \mathbf{A} (\Phi^{(k)}) \right] \mathbf{Y}^{(k)} = \mathbf{I} \mathbf{Y}^{(k)} \Lambda^{(k+1)}\tag{3.33}$$

Note that (3.33) is smaller in terms of problem size, compared to (3.26). That provides a significant advantage in terms of computational cost for solving the problem (Günel & Zoral, 2010).

A question might arise here about what the step size, $\Delta\epsilon$ and the number of solutions, N_0 should be. In fact, this choice mostly depends on the problem and no single answer can be given, but there is indeed a compromise between solution time and accuracy. It should be noted that the accuracy of the initial solutions has also major effect as well as the presence of spurious solutions. In the following chapter, performance of the method will be evaluated by numerical results.

CHAPTER FOUR

SOFTWARE DEVELOPMENT AND NUMERICAL RESULTS

4.1 Software Development

The performance evaluation of the step-by-step eigenvalue perturbation technique is made by implementing the method using Python (v2.7) scripting language. As it is seen in previous chapter, the step-by-step perturbation technique is heavily dependent on not only the results of FEM but also intermediary data used in FEM such as the matrices, the boundaries and the mesh structure. Unfortunately, commercially available common electromagnetic field solvers (e.g. Ansoft HFSS, CST Studio) don't provide this information to the user. Therefore, a FEM routine is written in the software. A Graphical User Interface (GUI) front-end is used to control the parameters and execute the operations. Software is mainly developed for Linux operating systems, but it is possible to adapt for other OS as well with slight modifications. Tests are performed on a machine which has the following specifications;

- Linux Mint 15
- Intel® Core™ i7 620M @ 2.67 GHz 64-bit CPU
- 6 GB RAM

Let us now further investigate the implementation of the methods as software routines.

4.1.1 FEM Routine

Prior to any mathematical operation, FEM requires the geometry to be discretized with mesh structures. Mesh generation is another problem by itself and it is irrelevant to the essence of the perturbation problem. Therefore, an open source software, namely Gmsh, is used for this purpose (Geuzaine & Remacle, 2009). Gmsh provides its own GUI to perform various operations like creating a geometry, mesh generation and visualization (Figure 4.1). Underlying processes are based on command line interactions with the operating system. In order to automatize the discretization process in FEM routine, command line interactions are favorable. There are two main steps for receiving the discretized geometry data in FEM routine;

1. Defining the structural properties of the geometry within the .geo file which is created previously.

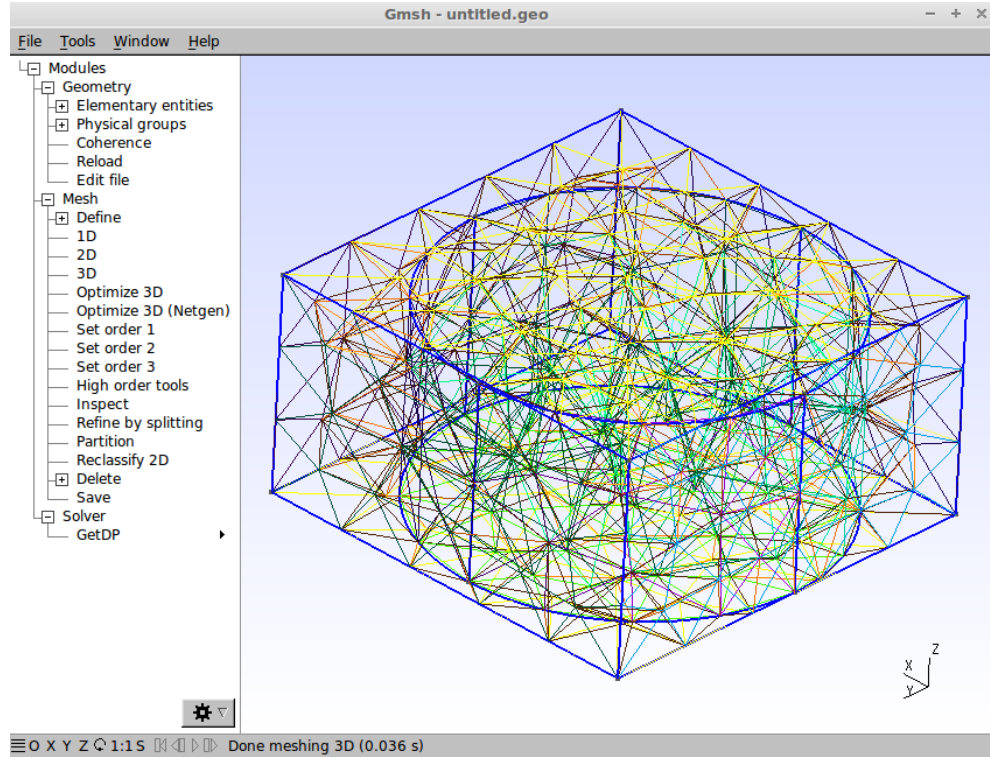


Figure 4.1 Gmsh GUI

2. Execution of mesh command in Gmsh, importing .msh file that is created by Gmsh in the FEM routine and reading the data.

An important parameter, discretization interval, is defined in the .geo file initially. Therefore, .geo file is partially modified within the FEM routine. Code is optimized for the geometries that are analyzed in this study and may require some modifications for different cases. There are two geometrical structures which are pre-defined, partially-filled rectangular cavity and rectangular cavity with cylindrical box.

After the geometrical data is obtained, the remaining FEM procedure is the same as given in the previous chapter. A flowchart which summarizes the operation is given in Figure 4.2.

Mathematical operations in FEM procedure, especially solving the eigenvalue problem, should be treated carefully for software implementation to meet the requirements in terms of time and accuracy. The major issue in this case is solving the eigenvalue problem since the entire FEM procedure up to solving the eigenvalue problem, which consists of meshing, reading data, creating interpolation functions and matrix assembly, can be completed in a few seconds while solving the eigenvalue problem may take several hours or even days to complete, depending on the number of

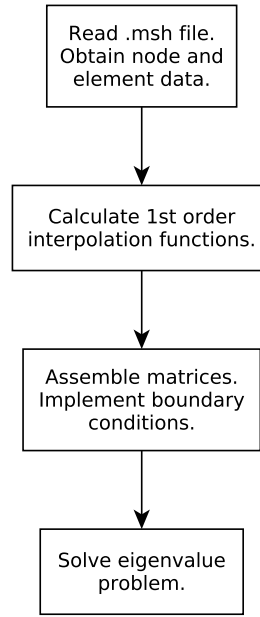


Figure 4.2 FEM routine flowchart for an eigenvalue problem

the unknowns and the system which executes the algorithm. Hence, it is essential to speed up the solution procedure of the eigenvalue problem. Besides choosing the optimum algorithm in terms of time and accuracy, one must also consider to execute the algorithm as fast as possible. Therefore, for the implementation of the numerical operations like norm, determinant, matrix addition-subtraction, augmentation, eigenvalue solution that the FEM procedure includes, SciPy and Numpy (Oliphant, 2007) libraries are used. The major contribution of these libraries is accelerating the solution of the eigenvalue problem by means of LAPACK linear algebra package and ARPACK (ARnoldi PACKage) eigenvalue algorithm package, which are written with FORTRAN in order to provide maximum speed. There are two functions used for solving the eigenvalue problem;

1. (scipy.linalg.eig): Finds all the eigenvalues and corresponding eigenvectors. Underlying algorithm is the QR algorithm which is based on QR factorization (Horn & Johnson, 1985). Computational cost of the algorithm is normally $\mathcal{O}(n^3)$. However, if the right-hand side matrix is in Hessenberg form, the cost is reduced to $\mathcal{O}(n^2)$ (Golub & Van Loan, 1996).
2. (scipy.sparse.linalg.eigs): Finds only specific number of eigenvalues which are smaller than some user-defined value. A tolerance parameter is used to limit the number of iterations. Function is based on Implicitly Restarted Lanczos Method (IRLM) (Calvetti et al., 1994). It is not always guaranteed all the eigenvalues,

which correspond to a resonant mode, to be found. Significantly faster than `scipy.linalg.eig` function for most cases.

A simple benchmark is performed by measuring the solution time of these two functions for different number of unknowns. Typical FEM matrices are used for the test. Results are given in Table 4.1. IRLM algorithm is executed with the following parameters; Number of eigenvalues: 30, Largest eigenvalue: 600000, Tolerance: 1.

Table 4.1 SciPy eigenvalue algorithms benchmark

		Number of unknowns				
		3555	2253	1620	813	165
Method	QR	939 secs	238 secs	72 secs	8.3 secs	0.22 secs
	IRLM	38 secs	12 secs	1.7 secs	0.97 secs	0.03 secs

According to the given information, the most convenient method to solve a problem is to use QR algorithm initially with a rough grid for having a perspective about the eigenvalues, then re-solving the problem with IRLM using a denser mesh to obtain more accurate results.

4.1.2 Step-By-Step Perturbation Routine

Step-by-step perturbation routine is closely dependent on the FEM routine and takes the following parameters as input arguments.

- Initial eigenvalues & eigenvectors
- Stiffness matrix
- Node table
- Boundary nodes
- Element (tetrahedra) table
- Geometry information (e.g. dimensions, regions)
- Amount of dielectric perturbation
- Number of perturbation steps
- Number of perturbation vectors (N_0)

NumPy and SciPy libraries are used in the perturbation routine as well and the eigenvalue function is `scipy.linalg.eig`, the same as used in the FEM routine. Thus, the time requirements of the perturbation process can be roughly estimated by referring to Table 4.1. Note that the method used here involves the solution of an eigenvalue problem, like given in (3.33), at each perturbation step. This resulted the step size variations unnecessary for improving the accuracy. On the other hand, observing the parametric history is also a major concern which requires the problem to be divided into several steps.

4.1.3 GUI

A dedicated GUI is designed to control FEM and perturbation parameters, initiate the process and observe the results of these processes. GUI is written by using wxPython library. There are two window classes defined for GUI structure.

1. Control Panel: Parameters for FEM and perturbation procedures are set, process is initiated (Figure 4.3).
2. Results Window: The eigenvalues and the corresponding resonant frequencies are listed in a table. Magnetic fields (eigenvectors) can be plotted. The eigenvalue history is provided for tracking the values, if perturbation is performed.

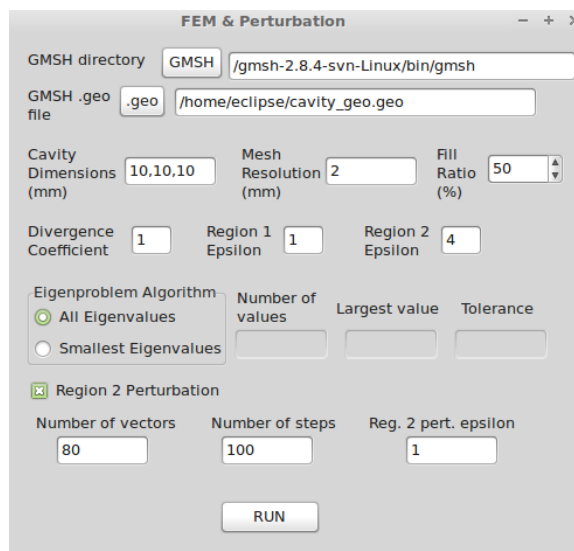


Figure 4.3 GUI control panel of the created software

It is possible to perform only FEM procedure by unselecting perturbation option. If the perturbation option is selected, FEM and perturbation procedures are executed

respectively, then two result windows appear after all operations are completed.

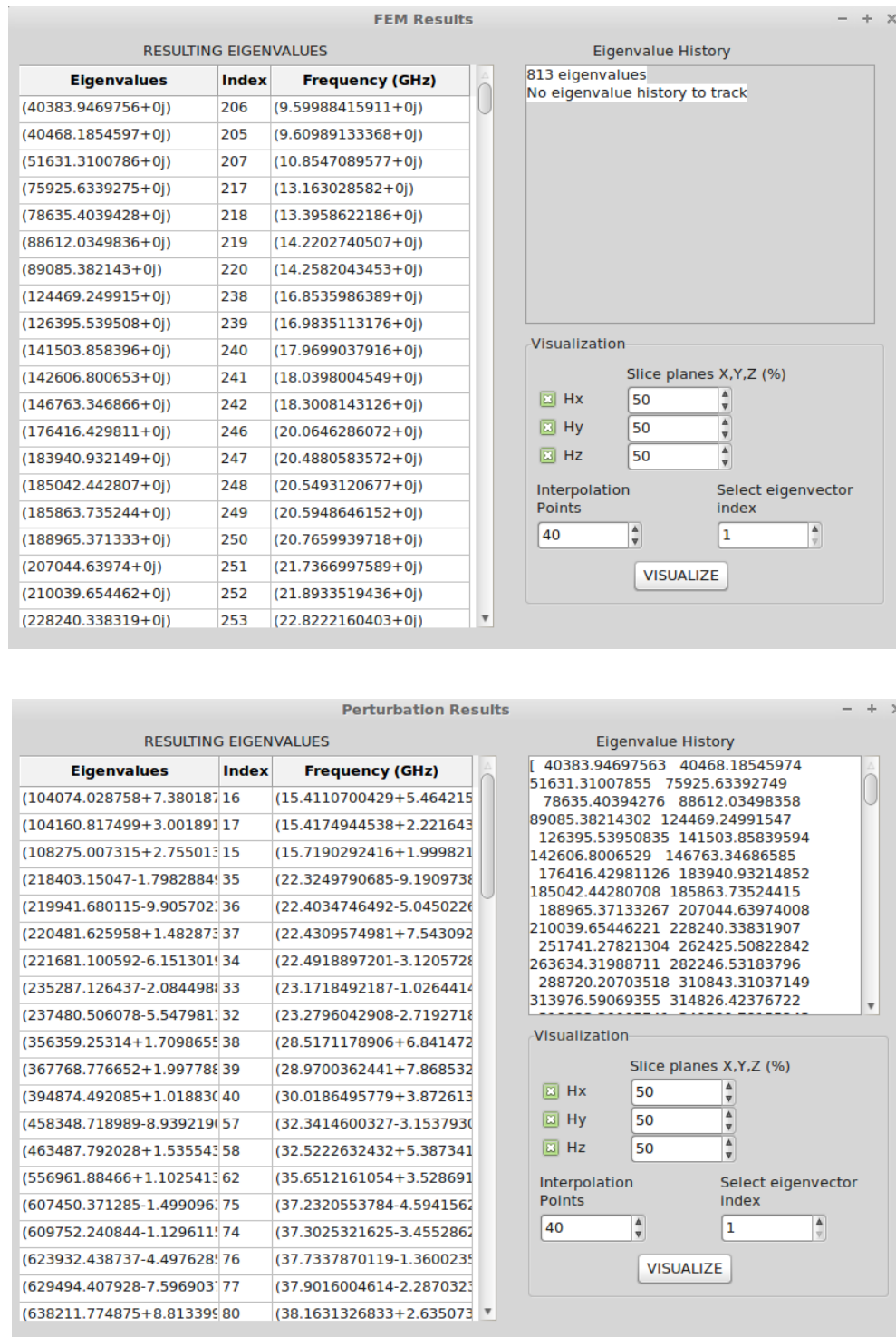


Figure 4.4 FEM and perturbation result windows of the created software

Noticable difference between FEM and perturbation result windows, as seen in Figure 4.4, is the eigenvalue history, which is present in perturbation results and

shows the information about eigenvalues at each perturbation step. Magnetic field components (eigenvectors) can be viewed as cross-sectional plots in both perturbation and FEM results. The field intensity plots are also available. Plotting operations are performed by exporting the data into .m files, then plotting it using Octave. Plotting operations are handled by system calls, hence, no user intervention is required to run Octave explicitly. A sample set of plots is shown in Figure 4.5.

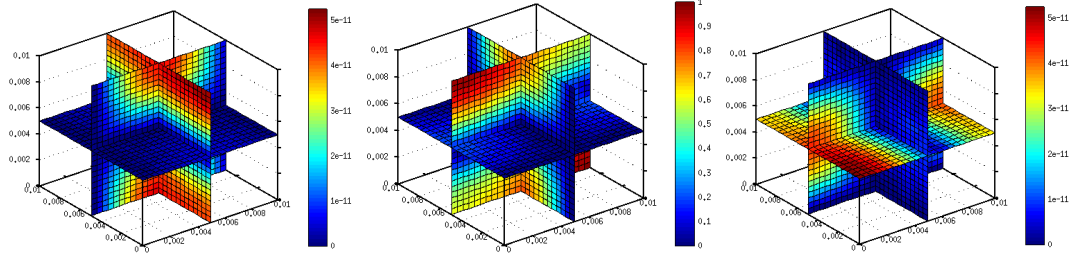


Figure 4.5 Magnetic field components (H_x , H_y , H_z) for $10 \times 10 \times 10$ mm cubic cavity

4.1.4 Future Work For Software

Current capabilities of the software are very limited due to external dependencies. As mentioned previously, there are lots of external libraries and software used in the development. The names and the versions of all libraries and software used in test and development are listed below.

- Eclipse 3.8.1
- PyDev 3.0.0.2
- Python 2.7
- Gmsh 2.8.4 Linux
- NumPy 1.7
- SciPy 0.11
- Octave 3.8.0
- wxPython 2.8.12

There are two major improvements which should be implemented. First, FEM and the perturbation procedures must be generalized to cover all kinds of geometries. This alteration also requires some modifications on GUI. Secondly, Octave dependency must be removed altogether. For plotting tasks, SciPy packages can be used. However,

data import and export from/to Octave can be optional for flexibility. It is not possible to remove NumPy and SciPy dependencies as they provide most critical resources for the solution of the main problem.

4.2 Numerical Results

The performance and the results produced by FEM and the step-by-step perturbation algorithm are affected by the nature of the problem and the parameters related with these methods. Thus, both FEM and the step-by-step perturbation method should be tested with the software that is described recently. Despite that the major concern of this study is to evaluate the performance of the step-by-step perturbation method, examining the outputs of the FEM implementation is critical as well since FEM provides the basis for the entire perturbation process.

Analysis is made by changing the software parameters and conditions, then observing their effects over the results. Two different cavity structures are used as test cases;

1. Uniformly filled cubic cavity
2. Partially filled cubic cavity

Results will be compared with Ansoft HFSS in several cases. Furthermore, the analytical solutions for the structures are also used for evaluating the performance with a solid reference.

4.2.1 FEM Results

FEM results will be examined for two parameters; mesh resolution and divergence coefficient against spurious solutions. A cubic cavity whose one side is 10mm and filled with vacuum ($\epsilon_r = 1$) is used as the test case. The analytical results for the resonant frequencies of the structure are given in Table 4.2.

Table 4.2 First 12 resonant frequencies of a cubic cavity with $10 \times 10 \times 10$ mm, $\epsilon_r = 1$

Mode	1	2	3	4	5	6	7	8	9	10	11	12
Freq (GHz)	21.213			25.981			33.541					36.742

4.2.1.1 Mesh Resolution

One of the most important parameters for the software, and for the FEM in general, is the size of the problem which is ultimately determined by the mesh structure. The higher the mesh resolution is, the more accuracy is obtained in the expense of longer solution time due to larger matrices. A general scheme for the variation of the solution time with respect to the number of unknowns is given in 4.1. Mesh resolution is determined by setting a characteristic length, which is defined for the individual points of the geometry and propagated throughout the structure during meshing process. Hence, elements are intended to be uniform, or at least similar in terms of shape and volume. However, it is possible for some grids to have tetrahedral elements whose edge lengths are much larger or smaller than the characteristic length, but it is a rare situation in general. Let us now demonstrate how the accuracy varies if the problem size increases due to denser meshing. Cubic cavity problem ($10 \times 10 \times 10 \text{ mm}$, $\epsilon_r = 1$) is solved by using QR algorithm for 4 different characteristic lengths; 5mm, 2mm, 1mm, 0.75mm. The resulting outputs are shown in Figure 4.6.

It can be noticed that a well-refined grid produce more accurate results as the pattern of the resonant frequencies is similar to the analytical solution, especially for 1 and 0.75mm characteristic lengths. It should be noted that the results given in Figure 4.6(c) and 4.6(d) are very close although the difference between their solution times is enormous where 1mm characteristic length produced 3500 unknowns, solved in 15 minutes and 0.75mm characteristic length did 8700 unknowns, solved in 6 hours. It is possible to solve the problem with IRLM algorithm using a denser grid, but it would be unnecessary for this and many similar cases. On the other hand, it has been observed that characteristic lengths beyond 0.6mm causes memory problems on the test machine, thus, it is not possible to implement altogether.

Presence of the spurious modes is evident for all cases and they occur as either multiple solutions near a real one or non-existent frequencies compared to the analytical results. Analyses are performed where divergence coefficient is set to 1, which has been beneficial for the elimination to a certain degree. Verifying the validity of the solutions might be possible by examining the field plots whether they show a meaningful pattern. Nonetheless, it is still possible for a spurious solution to have a field pattern similar to a real solution.

Eigenvalues	Index	Frequency (GHz)
(113674.0134+0j)	21	(16.1061673677+0j)
(123695.343958+0j)	14	(16.8011220712+0j)
(125103.505861+0j)	22	(16.8964843804+0j)
(272222.417027+0j)	28	(24.924333508+0j)
(281027.244923+0j)	23	(25.3242051969+0j)
(282760.984534+0j)	24	(25.4022013164+0j)
(283811.721904+0j)	31	(25.4493547317+0j)
(284251.490069+0j)	30	(25.4690640725+0j)
(291639.108394+0j)	29	(25.7979081335+0j)
(455445.110304+0j)	32	(32.2388567779+0j)
(512615.938555+0j)	33	(34.2024852031+0j)
(519517.73436+0j)	25	(34.4319643218+0j)
(674618.786917+0j)	46	(39.2365511751+0j)
(684534.052256+0j)	35	(39.5238406362+0j)
(688341.317553+0j)	34	(39.6336007666+0j)
(698469.968205+0j)	47	(39.9241317254+0j)
(840580.321792+0j)	50	(43.7976915202+0j)
(880796.902369+0j)	44	(44.8331754572+0j)
(892815.629956+0j)	52	(45.1380198585+0j)
(897443.076482+0j)	45	(45.2548434322+0j)

(a)

Eigenvalues	Index	Frequency (GHz)
(102011.045435+0j)	182	(15.2575643448+0j)
(102028.392964+0j)	183	(15.2588616053+0j)
(102474.443568+0j)	175	(15.2921797902+0j)
(216204.131808+0j)	193	(22.2123038476+0j)
(217072.615271+0j)	195	(22.2568721091+0j)
(217292.963286+0j)	194	(22.2681655964+0j)
(218194.834672+0j)	192	(22.3143295992+0j)
(222329.629458+0j)	187	(22.5247657455+0j)
(224207.044237+0j)	186	(22.619668592+0j)
(348395.898785+0j)	201	(28.1966898924+0j)
(348707.896998+0j)	200	(28.209312527+0j)
(352613.857836+0j)	191	(28.3668622073+0j)
(449362.761956+0j)	232	(32.0228625376+0j)
(451901.025878+0j)	233	(32.1131771162+0j)
(455983.586992+0j)	212	(32.2579092875+0j)
(592502.680951+0j)	258	(36.7711126137+0j)
(594070.744913+0j)	259	(36.8197380121+0j)
(597292.142962+0j)	260	(36.9194320916+0j)
(599088.359725+0j)	253	(36.9749037075+0j)
(600290.967141+0j)	261	(37.0119967337+0j)

(b)

Eigenvalues	Index	Frequency (GHz)
(99817.5037562+0j)	656	(15.0926313225+0j)
(99891.6450332+0j)	657	(15.098235446+0j)
(100036.584165+0j)	636	(15.10918497+0j)
(203357.343867+0j)	670	(21.5422737966+0j)
(203600.247156+0j)	669	(21.5551357061+0j)
(203621.272968+0j)	672	(21.5562486776+0j)
(203800.161752+0j)	673	(21.5657155778+0j)
(203912.691604+0j)	668	(21.5716685953+0j)
(203950.932494+0j)	671	(21.5736912285+0j)
(309003.53695+0j)	674	(26.5548184294+0j)
(311067.560746+0j)	681	(26.6433587663+0j)
(311281.075629+0j)	682	(26.6525011175+0j)
(413756.187634+0j)	712	(30.7279694083+0j)
(415509.350522+0j)	713	(30.7930006903+0j)
(415993.921044+0j)	698	(30.8109509874+0j)
(527461.467234+0j)	737	(34.6942081902+0j)
(527484.98718+0j)	742	(34.6949817034+0j)
(529137.710194+0j)	743	(34.7492925851+0j)
(529642.036339+0j)	745	(34.7658485804+0j)
(529750.564367+0j)	739	(34.7694103028+0j)

(c)

Eigenvalues	Index	Frequency (GHz)
(99286.220915+0j)	1718	(15.0524121531+0j)
(99302.4549585+0j)	1717	(15.053642694+0j)
(99380.2187286+0j)	1712	(15.0595357957+0j)
(200173.795484+0j)	1738	(21.3729870652+0j)
(200294.766902+0j)	1741	(21.3794442791+0j)
(200468.84236+0j)	1739	(21.3887326603+0j)
(200486.626714+0j)	1729	(21.3896813772+0j)
(200531.682061+0j)	1740	(21.392084693+0j)
(200548.169089+0j)	1728	(21.3929640669+0j)
(302830.935442+0j)	1747	(26.2882532562+0j)
(302954.527871+0j)	1762	(26.2936171363+0j)
(303233.72857+0j)	1763	(26.3057303497+0j)
(404359.193425+0j)	1776	(30.37702732+0j)
(404377.373022+0j)	1775	(30.3777101732+0j)
(405337.854316+0j)	1764	(30.4137655009+0j)
(509452.474649+0j)	1807	(34.0967864087+0j)
(509780.336182+0j)	1810	(34.1077562511+0j)
(510776.364338+0j)	1811	(34.1410605051+0j)
(510862.251199+0j)	1812	(34.1439307879+0j)
(511196.717003+0j)	1814	(34.1551061181+0j)

(d)

Figure 4.6 First 20 eigenvalues found by FEM routine for the tetrahedral characteristic lengths (a) 5mm (b) 2mm (c) 1mm (d) 0.75mm

4.2.1.2 Divergence Coefficient

Spurious modes are non-physical solutions which occur due to weak formulation of the governing differential equation in nodal FEM. In the previous chapter, a divergence term was written in the functional in order to force them towards higher frequencies,

which are much less of interest. The divergence term coefficient s from (3.21) is chosen as 1 for many cases as optimum (Jin, 2002). However, this should not always be a default choice since different values may produce better results, depending on the circumstances. Let us now demonstrate the effects of this coefficient by solving the cubic cavity problem with 4 different values, $s=0$, $s=0.5$, $s=1$, $s=1.5$. QR algorithm with 1mm characteristic length is used for the solution. In order to evaluate the results comparatively, the results obtained from Ansoft HFSS will be given first.

Ansoft HFSS Results: The eigenvalues and corresponding resonant frequencies obtained by HFSS is no different than the analytical solution. Results for the 12 modes with the lowest frequencies are given in Table 4.3.

Table 4.3 Lowest 12 resonant frequencies of a $10 \times 10 \times 10$ mm, $\epsilon_r = 1$ cavity found by HFSS

Mode	1	2	3	4	5	6
Freq (GHz)	21.201	21.201	21.202	25.969	25.969	33.529
Mode	7	8	9	10	11	12
Freq (GHz)	33.541	33.541	33.541	33.541	33.541	36.741

The magnetic field intensity on the walls of the cavity for the first mode (21.201 GHz) is shown in Figure 4.7.

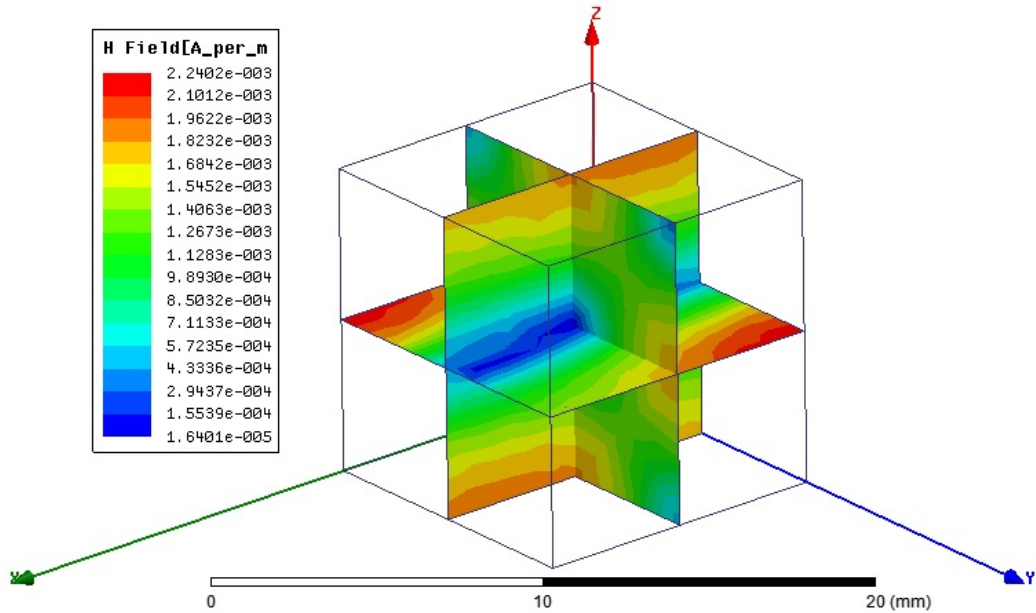


Figure 4.7 Magnetic field intensity plot from Ansoft HFSS for cubic cavity

$s=0$: Lack of any divergence term in the functional results many spurious modes to occur. There is no concentration near a single value, instead, eigenvalues are spread

over a wide interval of frequencies. Outputs between 20-25 GHz are shown in Figure 4.8. A serious problem with this case is the irregular field patterns occurring for each

Eigenvalues	Index	Frequency (GHz)
(178415.093348+0j)	1154	(20.177966968+0j)
(180325.670097+0j)	1155	(20.2857182081+0j)
(184458.520089+0j)	1156	(20.5168635895+0j)
(185488.214447+0j)	1157	(20.5740490691+0j)
(193977.088309+0j)	1158	(21.0395685184+0j)
(203012.140374+0j)	1159	(21.5239817925+0j)
(209029.821411+0j)	1160	(21.8406588745+0j)
(212890.479182+0j)	1161	(22.0414281504+0j)
(217374.640415+0j)	1162	(22.272350336+0j)
(221466.803277+0j)	1163	(22.4810157282+0j)
(230957.666396+0j)	1168	(22.9576696535+0j)
(240243.038555+0j)	1170	(23.414614776+0j)
(243497.229421+0j)	1171	(23.5726616721+0j)
(247700.187957+0j)	1172	(23.7752328512+0j)
(254300.628872+0j)	1173	(24.089918353+0j)
(257873.657634+0j)	1174	(24.258564678+0j)
(264071.79187+0j)	1175	(24.5483675525+0j)
(270814.983858+0j)	1176	(24.8598186288+0j)
(290573.516825+0j)	1186	(25.7507347789+0j)

Figure 4.8 Resonant frequencies for a cubic cavity ($10 \times 10 \times 10$ mm, $\epsilon_r = 1$) between 20-25 GHz for $s=0$

solution which makes impossible to identify whether a solution is spurious or not. Hence, $s=0$ is not a proper choice. The field plots for the mode at 21.5239 GHz are shown in Figure 4.9.

$s=0.5$: Larger values of the spurious coefficient results the solutions with smallest frequencies become closer to the actual resonant frequencies as expected since spurious modes are shifted towards higher frequencies, as shown in Figure 4.10.

The magnetic field intensity for the mode with 21.9117 GHz frequency is shown in Figure 4.11.

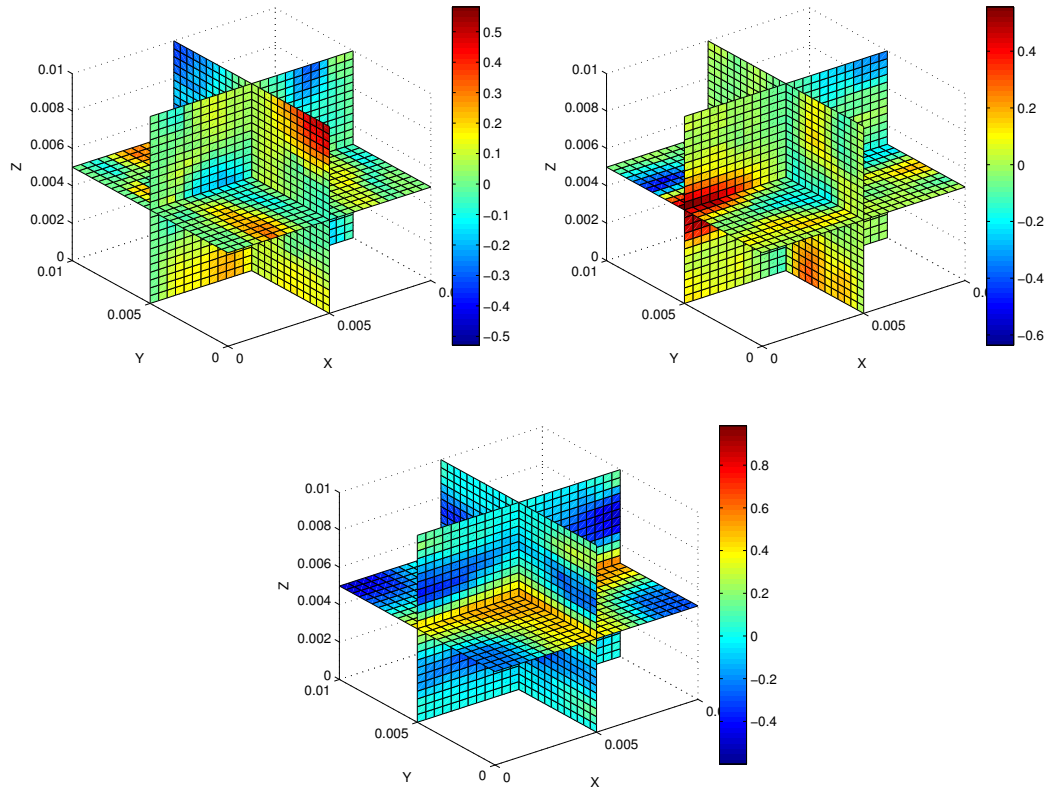


Figure 4.9 The field plots of H_x , H_y , H_z for $s=0$ at 21.5239 GHz

Eigenvalues	Index	Frequency (GHz)
(48016.7037927+0j)	745	(10.46785704+0j)
(48077.1100968+0j)	746	(10.4744393932+0j)
(48420.276617+0j)	744	(10.5117553373+0j)
(118600.26818+0j)	758	(16.4514600247+0j)
(119032.887576+0j)	760	(16.4814377904+0j)
(119259.638177+0j)	759	(16.4971284031+0j)
(181456.160188+0j)	775	(20.3492060446+0j)
(181609.460024+0j)	776	(20.3578000525+0j)
(182004.175268+0j)	777	(20.37991116+0j)
(189344.656541+0j)	778	(20.786823942+0j)
(194585.592696+0j)	779	(21.0725431473+0j)
(210393.642736+0j)	781	(21.9117930501+0j)
(210536.207522+0j)	780	(21.9192156153+0j)
(285935.172362+0j)	805	(25.5443820595+0j)
(287201.486159+0j)	806	(25.6008834483+0j)
(287868.217819+0j)	809	(25.6305821538+0j)
(288247.65143+0j)	808	(25.6474681823+0j)
(288989.278365+0j)	807	(25.6804409302+0j)
(294585.155525+0j)	810	(25.9278819225+0j)
(297129.922476+0j)	812	(26.0396298083+0j)

Figure 4.10 The smallest eigenvalues for $s=0.5$

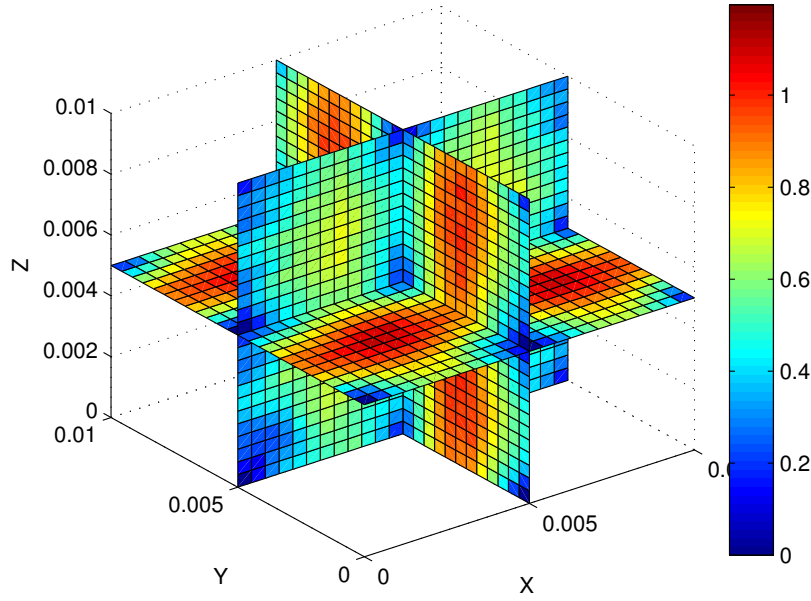


Figure 4.11 The magnetic field intensity plot for $s=0.5$ at 21.9117 GHz

The field pattern is not random anymore, but it is inconsistent with HFSS result. However, it can be inferred that the frequencies obtained from the process are much lower than they were supposed to be as the field pattern given in Figure 4.11 may belong to a mode whose mnp configuration is in the $22p$, $2n2$ or $m22$ form (2×2 peaks on the upper wall), which should have occurred at much higher frequencies.

$s=1$: The results for this case were actually given in Figure 4.6(c) and it was discussed that the frequencies are consistent with the analytical solution. However, the field patterns must also be investigated to validate the accuracy because of the mismatch between the field patterns and the resonant frequency of the solutions, like in the case of $s=0.5$. The magnetic field intensity plots of all 6 solutions near 21.5 GHz are given in Figure 4.12. The field intensity plots show some resemblance with HFSS result from certain cross-sectional views but don't match it completely. On the other hand, there are 6 solutions instead of 3 which leads the presence of spurious solutions. Intuitively, it can be claimed that increasing the divergence coefficient s , would eventually result correct number of modes with the correct field patterns because that was the situation when s is changed from 0 to 1. This assumption is theoretically correct since the real solutions correspond to physically existent electromagnetic fields whose divergence is equal to zero in source-free region. Thus, increasing the divergence parameter s should have no effect over the real solutions. However, that is not the case in practice.

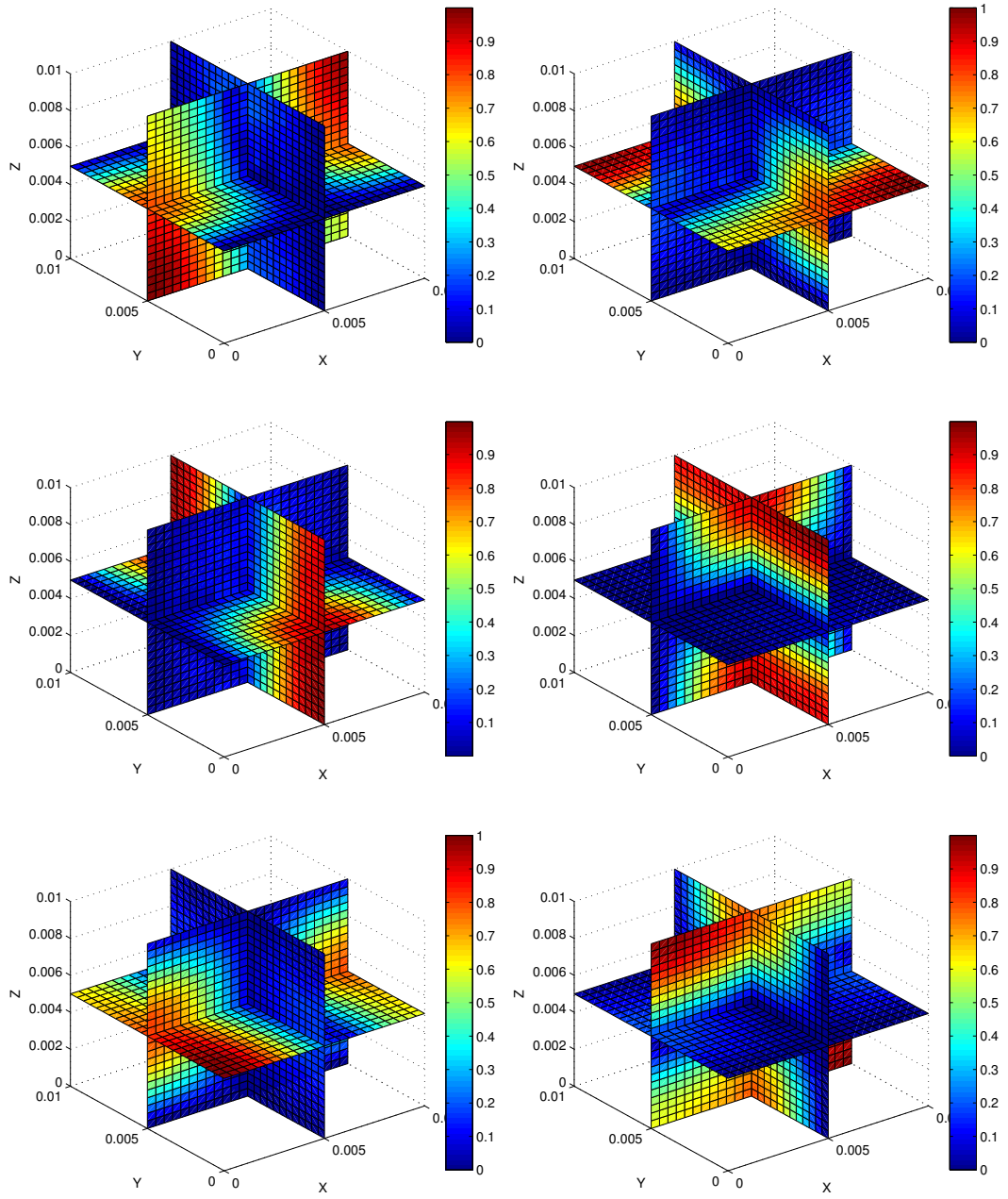


Figure 4.12 The magnetic field intensity plots of 6 eigenvalues near 21.5 GHz for $s=1$

$s=1.5$: Further increase in divergence coefficient results with a frequency shift for all solutions, as shown in Figure 4.13. The amount of shift is larger for spurious solutions, as expected. Three modes, occurred near 22.5 GHz and having index numbers 686, 687, 688 are those dominant modes that should have been near 21 GHz. Following three modes, near 25 GHz, are the spurious that were found near 21 GHz in the previous configuration. Those which should have occurred at 25 GHz ideally, are located near 27 GHz. Field patterns for the three modes near 22 GHz are shown in Figure 4.14. The similarity between the field patterns is noticeable compared to previous cases, but

Eigenvalues	Index	Frequency (GHz)
(148514.198763+0j)	670	(18.4096528562+0j)
(148641.787986+0j)	671	(18.4175590667+0j)
(149001.091415+0j)	669	(18.4398054956+0j)
(222207.992741+0j)	686	(22.5186032439+0j)
(222967.345772+0j)	688	(22.5570469239+0j)
(223049.227588+0j)	687	(22.5611884326+0j)
(282240.174935+0j)	696	(25.37879673+0j)
(282717.733611+0j)	695	(25.4002584906+0j)
(282942.902179+0j)	697	(25.4103714068+0j)
(327521.715966+0j)	708	(27.3389393372+0j)
(331257.611934+0j)	710	(27.4944188431+0j)
(421427.398428+0j)	722	(31.0115158063+0j)
(556499.568304+0j)	753	(35.636416563+0j)
(559534.612274+0j)	754	(35.733461583+0j)
(560595.091444+0j)	755	(35.7673081517+0j)
(561686.185593+0j)	756	(35.8020984403+0j)
(565717.367962+0j)	758	(35.9303433256+0j)
(566692.072164+0j)	757	(35.9612831434+0j)
(607575.17525+0j)	759	(37.2358799455+0j)
(609734.856091+0j)	760	(37.3020003892+0j)

Figure 4.13 The smallest eigenvalues for $s=1.5$

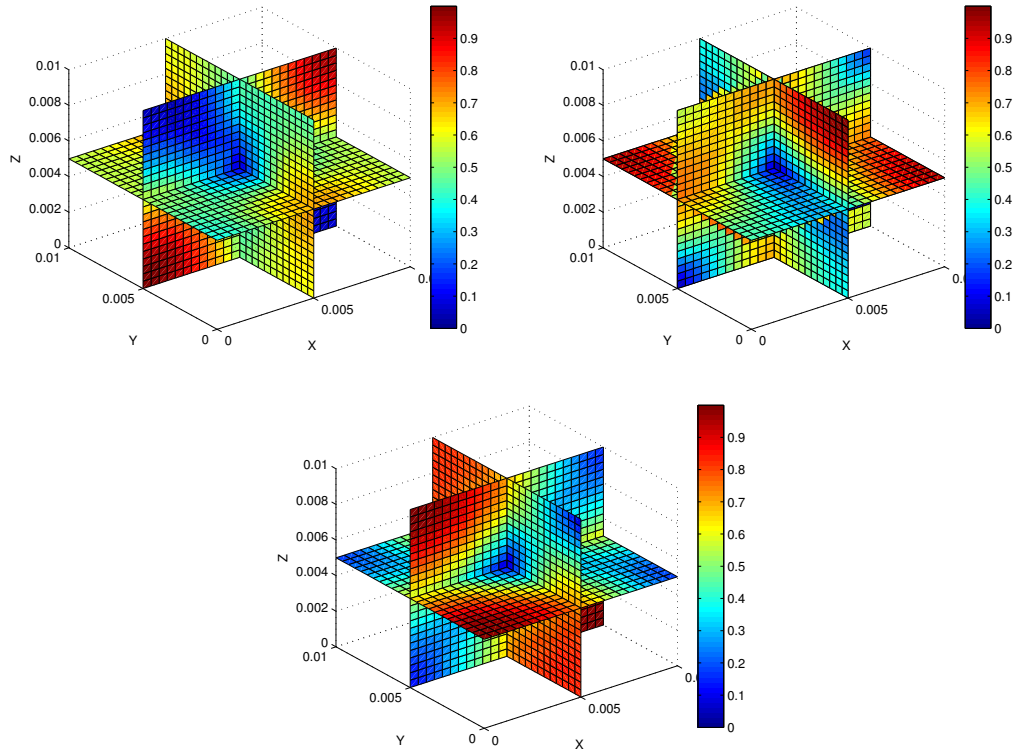


Figure 4.14 The field plots of the modes for $s=1.5$ near 22.5 GHz

$s=1.5$ is not used for the step-by-step eigenvalue perturbation process, instead, $s=1$ is used. This is mostly due to performance evaluation of the perturbation method would be easier when eigenvalues are inspected instead of field quantities. Since the accuracy of the eigenvalues produced by FEM routine is highest for $s=1$, this choice is logical. It is still possible to improve the accuracy by increasing the mesh resolution. Figure 4.15 shows the resulting eigenvalues for $s=1.5$ and characteristic length is 0.75mm. The

Eigenvalues	Index	Frequency (GHz)
(147797.041064+0j)	20	(18.365150036+0j)
(147871.711581+0j)	19	(18.3697887015+0j)
(148083.250284+0j)	18	(18.3829235077+0j)
(214104.934677+0j)	15	(22.1042075346+0j)
(214228.44103+0j)	17	(22.1105820175+0j)
(214524.514345+0j)	16	(22.1258556501+0j)
(282792.718928+0j)	12	(25.4036267267+0j)
(283605.834694+0j)	13	(25.4401221192+0j)
(283724.665795+0j)	14	(25.4454512781+0j)
(316266.381789+0j)	11	(26.8650792496+0j)
(317286.551415+0j)	10	(26.9083732473+0j)
(420653.787169+0j)	9	(30.9830389228+0j)
(532267.735199+0j)	8	(34.8519178371+0j)
(532664.67011+0j)	7	(34.8649107012+0j)
(533143.397414+0j)	6	(34.8805744359+0j)
(533602.28437+0j)	5	(34.8955824038+0j)
(535021.12352+0j)	4	(34.9419449768+0j)
(535672.094926+0j)	3	(34.9631958128+0j)
(598151.450605+0j)	2	(36.9459800282+0j)
(598404.51724+0j)	1	(36.9537947765+0j)

Figure 4.15 The smallest eigenvalues for $s=1.5$, characteristic length=0.75mm

results for two cases given in Figures 4.13 and 4.15 respectively, differ by only small margins whereas the time and memory requirements for the second case are several times larger than the first one. Although the problem is solved by IRLM algorithm in a relatively short time, prior knowledge about the solution is essential. It is unlikely to have such valuable information for every cavity problem as many of them don't have any analytical expression for the solution or can't be analyzed with FEM in a short while. Further increase in the mesh resolution could improve the situation but this resulted malfunction on the test computer, as indicated before. Ultimately, diminishing the effects of the large spurious coefficient values by increasing the mesh resolution, is not feasible.

4.2.2 Step-By-Step Eigenvalue Perturbation Results

The performance evaluation of the step-by-step perturbation method is mainly carried out by varying two parameters; the number of the perturbation steps and the number of the eigenvalues/eigenvectors tracked in the process. Additionally, limitations of the perturbation process and the effects of the spurious modes are also presented. A partially filled cavity is used as the test case for verification, due to having an analytical expression for its resonant frequencies, as given in Chapter 2. Ansoft HFSS will be also used as reference. Common parameters used for the cavity can be described as, $10 \times 10 \times 10$ mm dimensions, %50 fill ratio, normal vector of the interface plane towards \hat{z} direction (see Figure 2.2), first region relative permittivity $\epsilon_{r1}=1$, second region relative permittivity (perturbation parameter) is varied such that $1 \leq \epsilon_{r2} \leq 10$. FEM parameters are chosen as; $s=1$, characteristic length=1mm. It can be noticed that the dielectric variation of the second region ($1 \leq \epsilon_{r2} \leq 10$) where $\epsilon_{r1}=1$, correspond to the homogeneous cavity case for either in the beginning or in the end of the perturbation. Analysis for this case has been given previously. The results for the opposite case where $\epsilon_{r2}=10$ should also be given before the perturbational analysis.

Resonant frequencies of the partially filled cavity structure can be obtained by using the characteristic equations given in (2.22) and (2.24). Unfortunately, resonant frequency cannot be expressed explicitly like (2.8), therefore, roots of the characteristic equations are obtained numerically by locating the zero-crossing points of the sampled curve.

Table 4.4 Lowest 12 resonant frequencies of a $10 \times 10 \times 10$ mm, $\epsilon_{r1} = 1$, $\epsilon_{r2} = 4$ partially filled cavity

Mode	1	2	3	4	5	6
Freq (GHz)	12.52		15.01		18.8	20.38
Mode	7	8	9	10	11	12
Freq (GHz)	20.38		23.18	24.4	25.07	25.58

Partially filled cavity has lower resonant frequencies compared to vacuum filled cavity, as expected. Analyzing the same structure by using HFSS, shows an interesting result, as given in Table 4.5.

Table 4.5 Lowest 21 resonant frequencies of the partially filled cavity obtained from HFSS

Mode	1	2	3	4	5	6	7
Freq (GHz)	12.455	12.527	12.528	15.02	18.13	18.134	18.837
Mode	8	9	10	11	12	13	14
Freq (GHz)	18.848	20.428	20.443	22.369	23.214	23.225	24.532
Mode	15	16	17	18	19	20	21
Freq (GHz)	24.756	24.789	25.131	25.356	25.697	25.703	26.458

The number of the resonant frequencies is higher in HFSS' results for the same interval and these frequencies seem to be degenerate with other modes. Thus, the number of the resonance modes for the same frequency interval is higher in HFSS' results. This is not a major problem if only the frequencies where resonance occur, are sought. However, it should be known that these additional solutions also correspond to the physically existent modes and they are most likely in hybrid form.

4.2.2.1 Number of Perturbation Steps

Main motivation behind the step-by-step perturbation method is to divide the total variation into smaller steps where the amount of perturbation is large. Consequently, the number of the perturbation steps is a trade-off between solution time and accuracy. It should be noted that the amount of the total perturbation is also critical due to affecting the step size, which is actually the main parameter related with the accuracy. Hence, all the tests are performed with the same amount of total perturbation. Let us now demonstrate the results of three different perturbation process where the number of the initial eigenvectors is 40 (total eigenvectors: 3555), number of perturbation steps are chosen as 5, 20, 80 and relative permittivity of the perturbation region is varied from 4 to 1. The results are given as the variation of the resonant frequencies for a certain mode with respect to the relative permittivity of the perturbation region, in Figure 4.16. Variation of the analytical solution is also given for comparison. Mode number is arranged such that the dominant mode, either TM_{110} or TE_{011} or TE_{101} , is tracked. The figures indicate that all three cases have similar characteristics. Resonant frequencies are always higher than the analytical results for all cases. The average errors between the analytical and the perturbation solutions are 713, 717, 738 MHz for 80, 20, 5 steps, respectively. That implies the accuracy gets better when the number of steps are increased, the differences are barely visible though. On the other hand, time requirements increase linearly with respect to the number of steps. Nonetheless, the

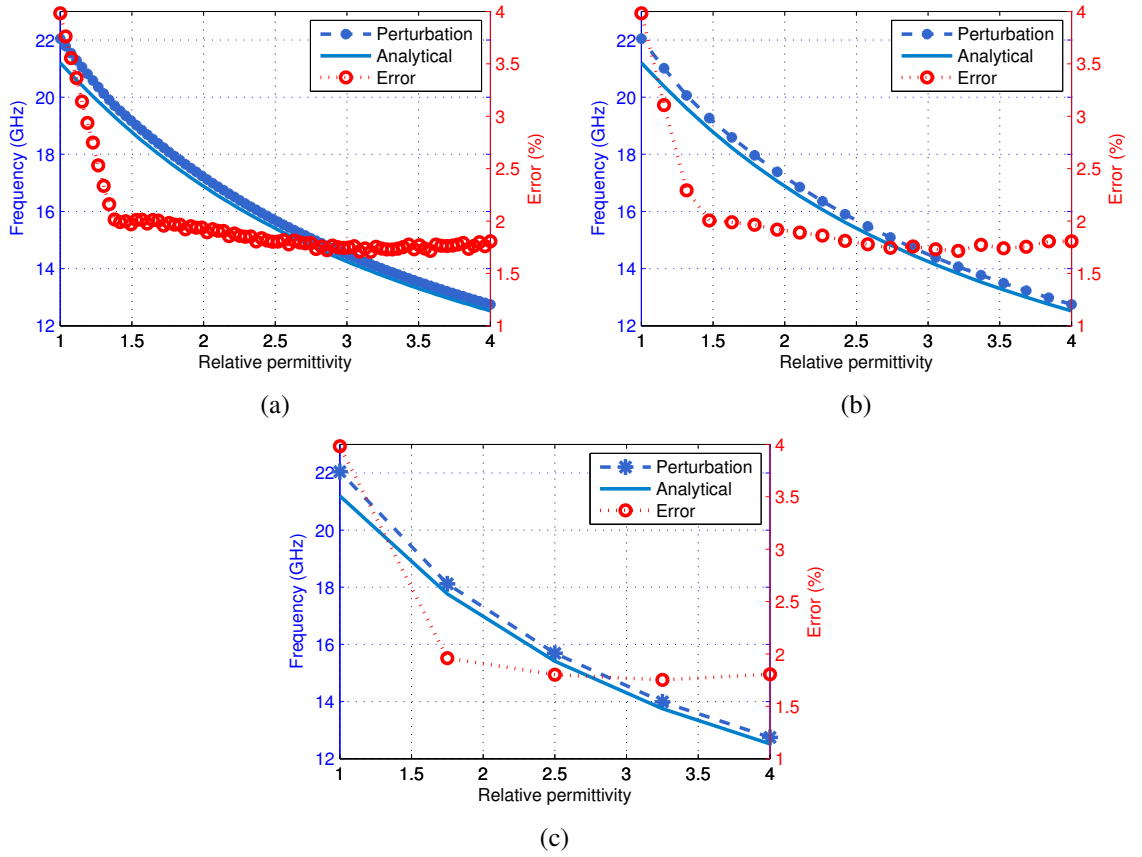


Figure 4.16 Perturbation analysis of the partially filled cavity by (a) 80 steps (b) 20 steps (c) 5 steps, from $\epsilon_{r2}=4$ to 1

step-by-step perturbation procedure does not take a long time to complete in general as the longest time measured was 118 seconds for 80 steps.

4.2.2.2 Eigenvalue Identification & Perturbation Interval

It should be noted that no restriction or condition has been given about the eigenvalues or the perturbation process' itself in the recent analysis but the accuracy of the results mostly depends on to identify the correct eigenvalues and to realize the limitations of the perturbation process. Let us now give an example where the process is reversed such that the relative permittivity of the perturbation region is incremented. Figure 4.17 shows the results for perturbation where the relative permittivity of the perturbation region is initialized from 1, finalized at 4 and 10, total number of steps are 5 and 20.

Figure 4.17 shows that the error between the analytical and the perturbation results increase with respect to the relative permittivity, on the contrary of the previous case.

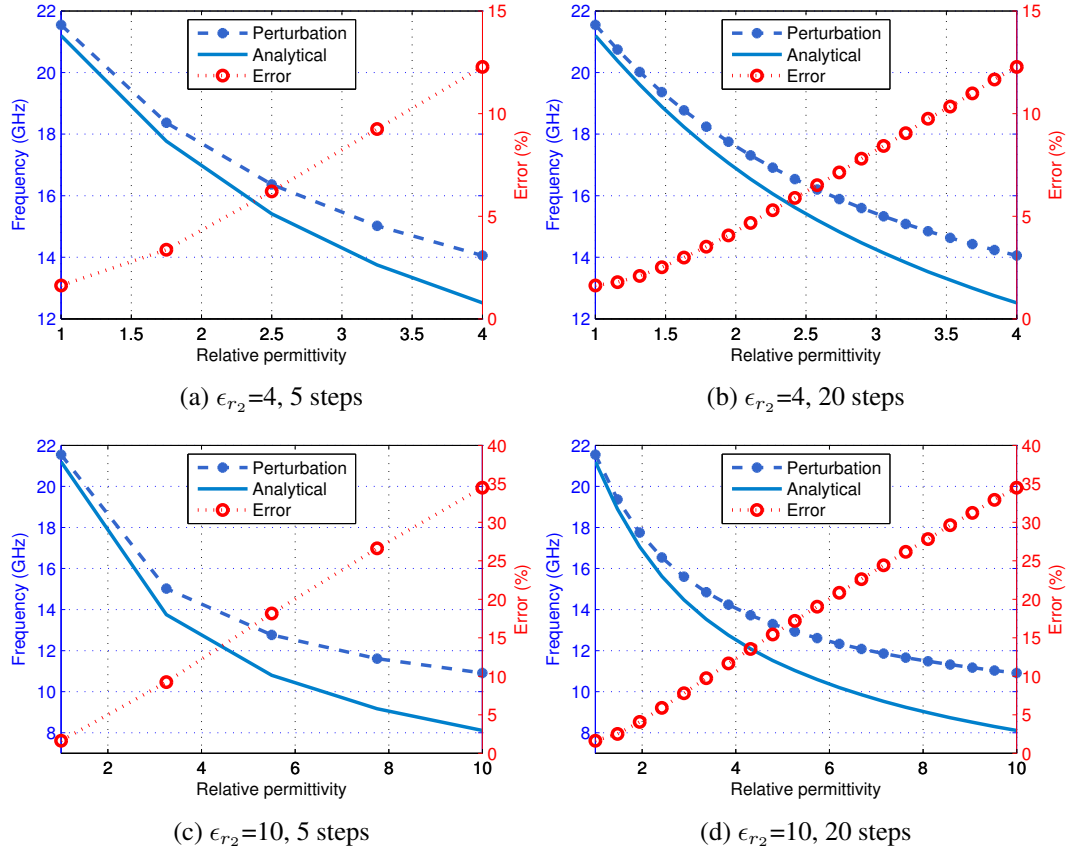


Figure 4.17 Perturbation analysis from $\epsilon_{r_1}=1$ to $\epsilon_{r_2}=4, 10$ by 5, 20 steps

Additionally, increased number of perturbation steps had no visible benefit in terms of accuracy. Therefore it can be deduced that a wrong choice of eigenvalue has been made for representing the mode, despite that there was no significant error initially. Furthermore, it is possible that different eigenvalues may align with the analytical solution at different parts of the perturbation interval. This argument can be justified by investigating the variations of the different eigenvalues. Figure 4.18 shows the perturbation results for two different eigenvalues along with the same mode.

Results in Figure 4.18 indicate that the variation of the eigenvalues may not align with the ideal solution throughout the perturbation interval. The eigenvalue given in Figure 4.18(a) match the ideal result at the end of the interval and the eigenvalue in Figure 4.18(b) does at the beginning. From the user perspective, it may not be possible to identify the correct perturbation solution since there might not be a reference (i.e. analytical solution) to compare. Investigating the characteristics of multiple eigenvalues can provide useful information though. Figure 4.19 shows the variation of 9 eigenvalues during the perturbation process.

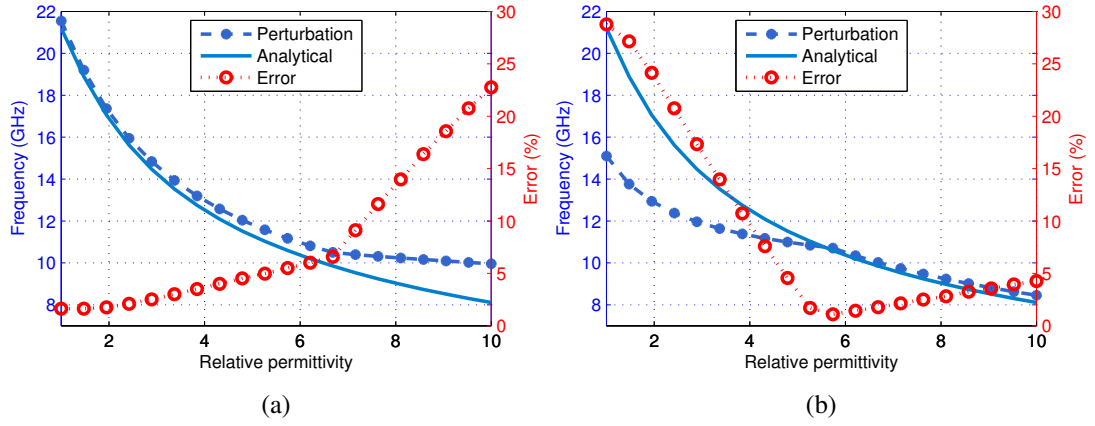


Figure 4.18 Deflection of eigenvalues during the perturbation process

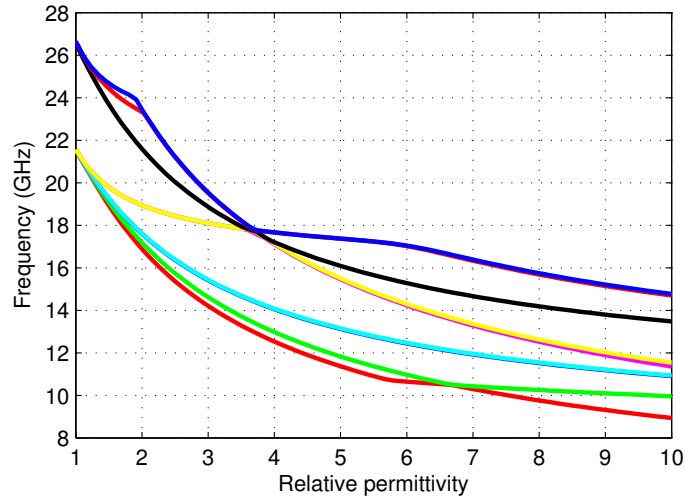


Figure 4.19 Variation and deflection of nine eigenvalues during the perturbation process

It can be noticed that the larger the perturbation interval is, the more likely to observe a cross-pass between the curves. This is an important limitation in terms of the total amount of perturbation that can be implemented without losing the accuracy. A possible solution for this problem is to investigate the derivatives of the characteristic curves whether they are smooth functions or not. If the derivative of a curve has a sharp transition at some point, remaining parts of the curve would probably lead erroneous results.

4.2.2.3 Number of Eigenvalues

Being able to reduce the problem size is a major advantage of the step-by-step perturbation technique. Deciding the number of eigenvalues is a trade-off between time and accuracy, as usual. However, time requirements for the step-by-step perturbation

technique are not extreme, therefore, accuracy is the primary concern. Test are performed with 40 perturbation steps, relative permittivity variations from 4 to 1, 1 to 4, 1 to 10 and the number of the eigenvalues used in the perturbation is set as 20, 80 respectively. Results are shown in Figures 4.20, 4.21 and 4.22, respectively.

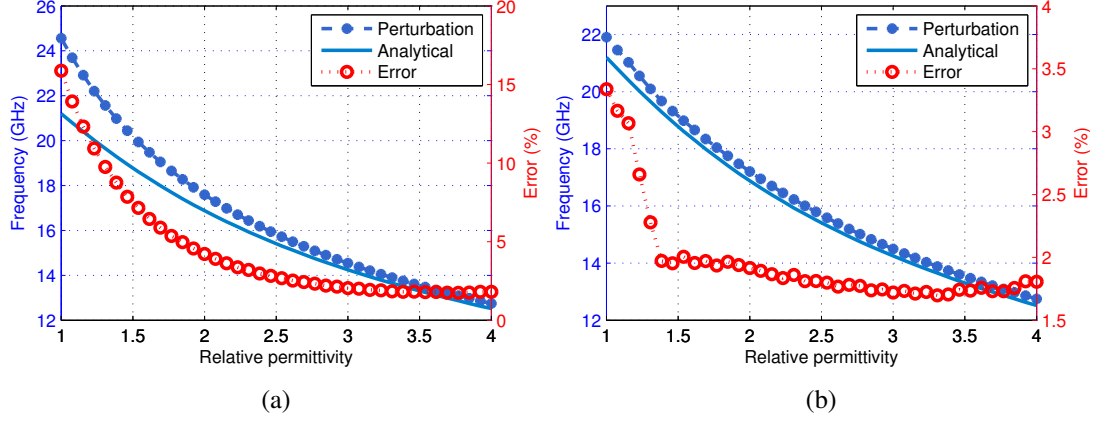


Figure 4.20 Effects of number of initial eigenvalues for (a) 20 (b) 80 , ϵ_{r2} is perturbed from 4 to 1

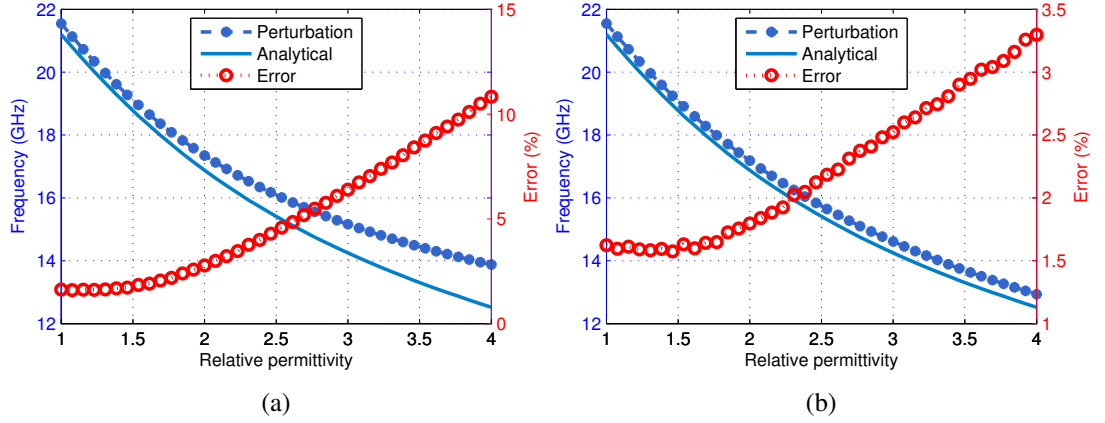


Figure 4.21 Effects of number of initial eigenvalues for (a) 20 (b) 80 , ϵ_{r2} is perturbed 1 to 4

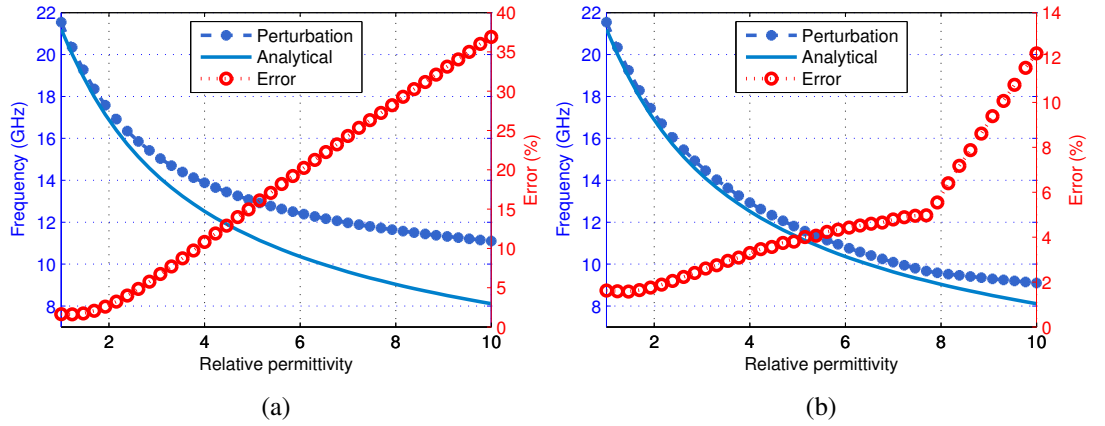


Figure 4.22 Effects of number of initial eigenvalues for (a) 20 (b) 80 , ϵ_{r2} is perturbed 1 to 10

The differences are evident as the accuracy increases with the number of the eigenvalues. Correct choice of the eigenvalue for representing the mode of interest is essential here too. The eigenvalues are selected with respect to the resonant frequencies they represent.

4.2.2.4 *Effects of Spurious Solutions*

Elimination of certain spurious solutions from the step-by-step perturbation process requires prior identification. It has been shown that introducing a divergence term in the FEM formulation has some benefits for identifying the spurious modes at lower frequencies. However, the size of the set of perturbed eigenvalues generally far exceeds the number of eigenvalues which can be identified by including the divergence term. Therefore, different methods are required for higher frequency region. Although there is no formula to identify the spurious modes with %100 accuracy, it is possible to use various methods in order to have a rough idea. Fundamentally, spurious modes don't correspond to any physically existent electromagnetic field, thus, they cannot satisfy Maxwell' equations. In fact, no solution obtained by FEM could exactly satisfy Maxwell' equation because of approximations. However, the spurious modes would have rather larger errors compared to the real solutions, hence, they might be distinguished. The reason for including the divergence term in the functional is based on this fact. Considering Maxwell' equations, it can be stated that the spurious solutions will have larger errors for Helmholtz' equation, too. Moreover, the error term obtained for Helmholtz' equation is equal to the energy at a chosen point. If the energy is integrated in the elements of the FEM grid, a new error criteria, related with energy densities of the elements, is obtained. Investigating these error terms, namely divergence error, point-wise energy and energy density, gives an insight about the characteristics of the solutions. Divergence and point-wise energy terms are calculated at the centroids of each tetrahedral element, then. Similarly, energy density term is also calculated for each element. This procedure is repeated for each mode and the error of a certain mode is simply the sum of the errors calculated for individual elements. Mathematical representations of the error terms are given below.

1.
$$\sum_{i=1}^{N_e} ||\nabla^2 \mathbf{H}(x_i, y_i, z_i) + \beta^2 \mathbf{H}(x_i, y_i, z_i)||^2 = 0 \quad \text{where } x_i, y_i, z_i \text{ are the coordinates of the centroid of } i\text{th element (Pointwise energy).}$$
2.
$$\sum_{i=1}^{N_e} \left| \int_{V_i} (\nabla^2 \mathbf{H} + \beta^2 \mathbf{H}) dV \right|^2 = 0 \quad \text{where } V_i \text{ is the volume of the } i\text{th element (Energy density).}$$

$$3. \sum_{i=1}^{N_e} |\nabla \cdot \mathbf{H}(x_i, y_i, z_i)|^2 = 0 \quad \text{where } x_i, y_i, z_i \text{ are the coordinates of the centroid of } i\text{th element (Divergence).}$$

where N_e is the number of elements in the mesh structure. It should again be noted that these error terms must be calculated for each mode individually. A key point about the energy terms is the reduction of the norm expression such that the $\nabla^2 \mathbf{H}$ term is equal to zero for each element since the second derivative of a linear function, which we implement for interpolation, is also zero. Hence, the expressions are reduced to the norms of the field expressions, which represent the energy.

Initial FEM solution is made where $\epsilon_{r1} = \epsilon_{r2} = 1$ hence, corresponds to the uniformly filled cavity problem which has been analyzed previously. Divergence coefficient s is chosen as 1. Relative dielectric permittivity of the perturbation region is varied from 1 to 4 in 20 steps. The error plots for the 100 modes with lowest frequency are given in Figure 4.23.

Characteristics of the plots related with energy, are quite similar but the divergence term is significantly different. It is not possible to claim that one of the plots provides more accurate results since there are evidences to support the validity for each plot. Therefore, elimination is performed by identifying the modes which are deviated (abrupt peaks) from the general trend, in any one of the error plots. The modes with the index number of 1, 2, 3, 8, 13, 14, 15, 27, 43, 44, 46 are labeled as spurious. Total number of eigenvalues selected for perturbation is 80. It should be emphasized that labeling is done manually and no automatic process is used for this purpose as it would bring its own challenges like determining the correct threshold, which are out of the scope of this study. Now let us compare the perturbation results for the cases where these labeled modes are included and excluded, respectively.

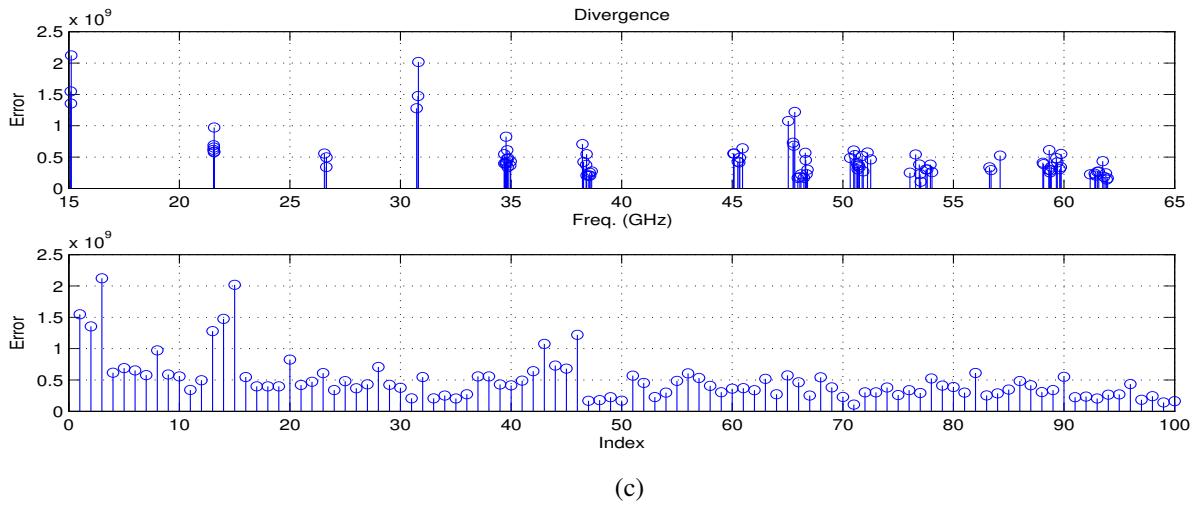
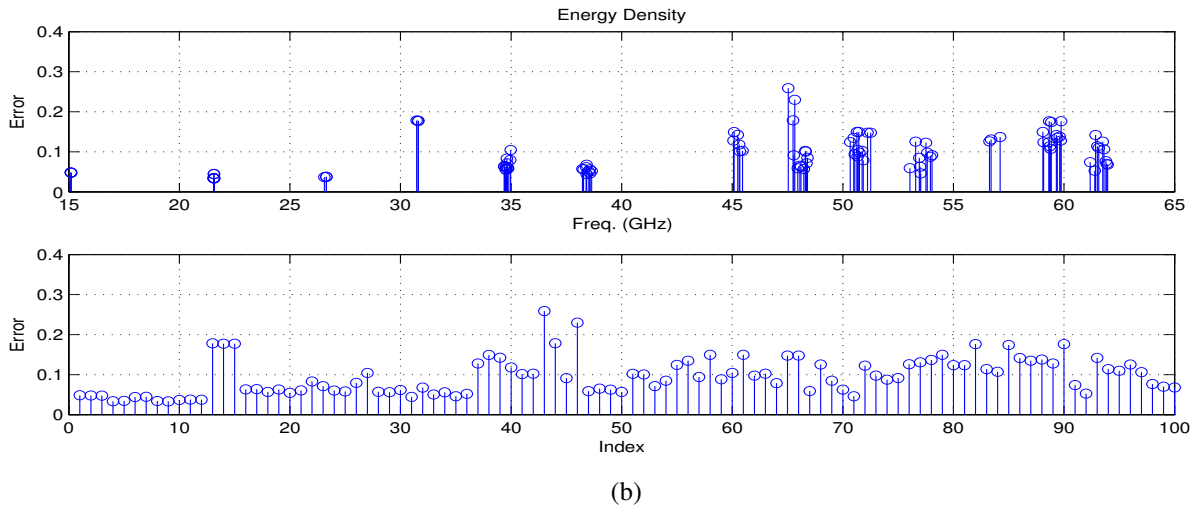
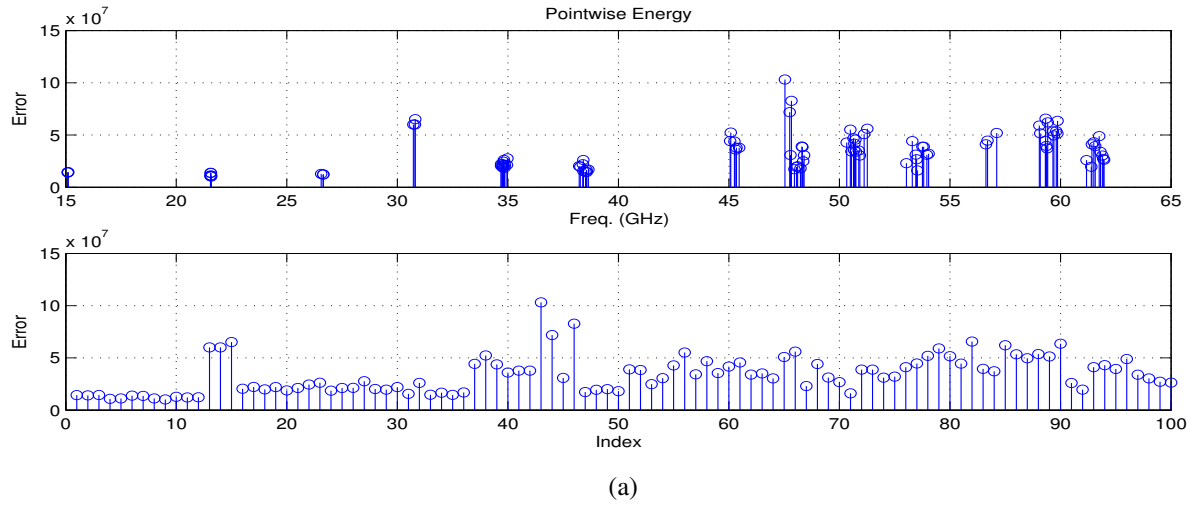


Figure 4.23 FEM errors calculated by (a) Point-wise energy (b) Energy density (c) Divergence for the elimination of the spurious modes

Figure 4.24 shows the plots of the error terms for 25 modes with the lowest frequencies, without any spurious mode exclusion. Mean values of the point-wise energy, energy density and divergence term are 1.16×10^7 , 3.55×10^{-2} , 1.07×10^9 , respectively. A key point about the error calculation is that the eigenvectors should have been unnormalized during the perturbation process.

Figure 4.25 shows the new situation of the perturbation results when the labeled eigenvalues are excluded from the process. Mean values of these new error terms also support the statement as they are found as 0.88×10^7 , 2.61×10^{-2} , 0.51×10^9 , respectively. Decline of the errors is evident from both figures and the numerical values, especially for the divergence term. It can also be noticed that the elimination of certain eigenvalues have prevented spurious solutions to re-occur in some regions. For example, the first 3 modes in the solutions of Figure 4.24, which are most likely spurious, don't appear in Figure 4.25 where some eigenvalues were excluded. As a result, frequency spectrum of the solution has also improved.

A final remark about the perturbation errors is the comparison of the results with native FEM solution. Experiments showed that the error values are 0.63×10^7 , 1.93×10^{-2} , 0.63×10^9 for point-wise energy, energy density and divergence term respectively. It is surprising to see that the divergence error of the perturbation solution where initial filtering is performed, is slightly lower than the FEM solutions'. This is due to the errors introduced by spurious solutions probably far exceeds the numerical errors of the entire perturbation process.

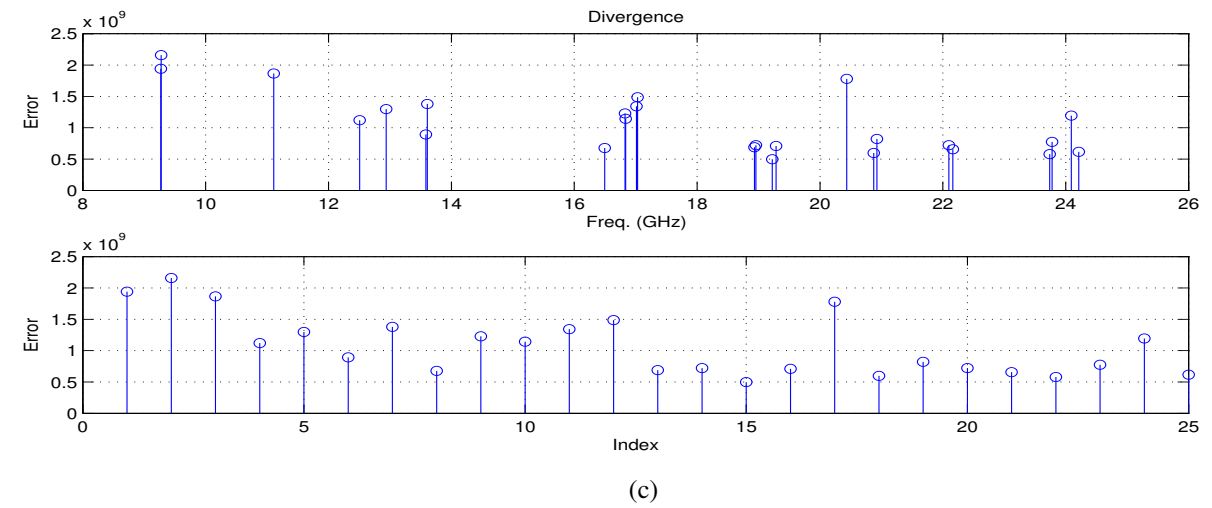
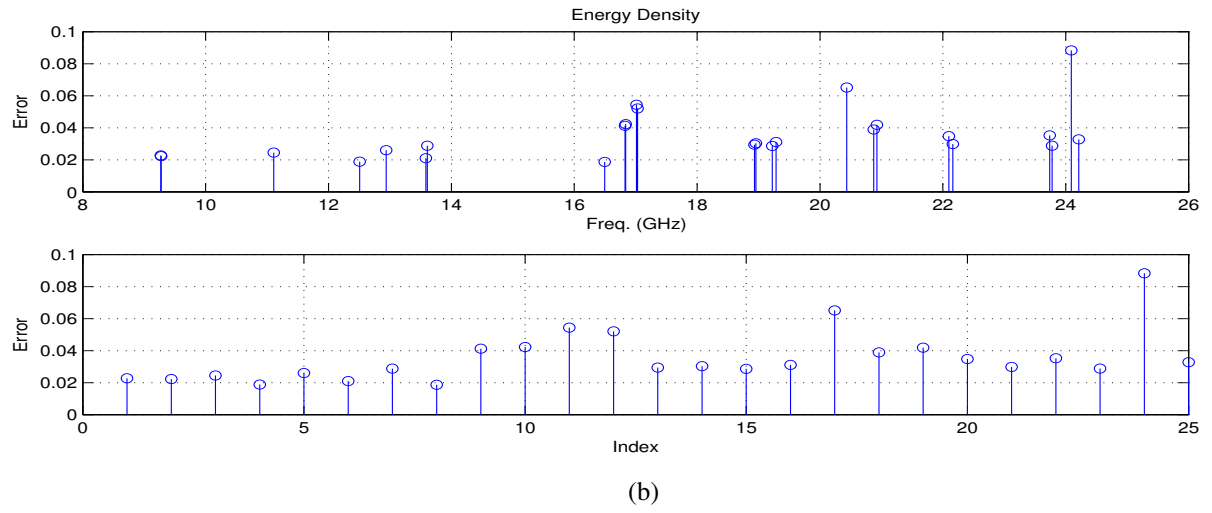
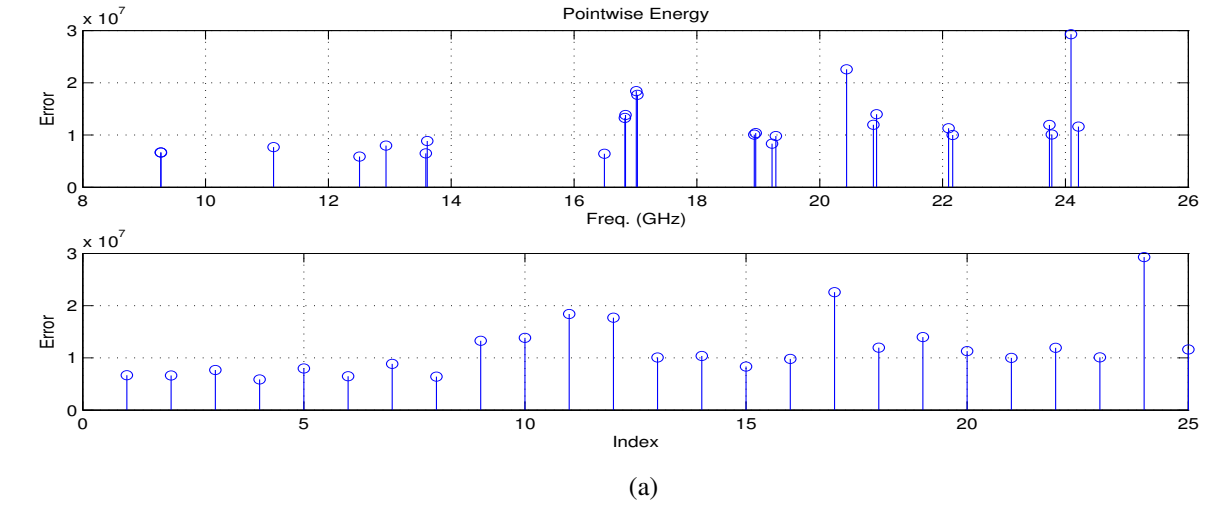


Figure 4.24 Errors of 25 modes without spurious exclusion calculated by (a) Point-wise energy (b) Energy density (c) Divergence obtained from perturbation

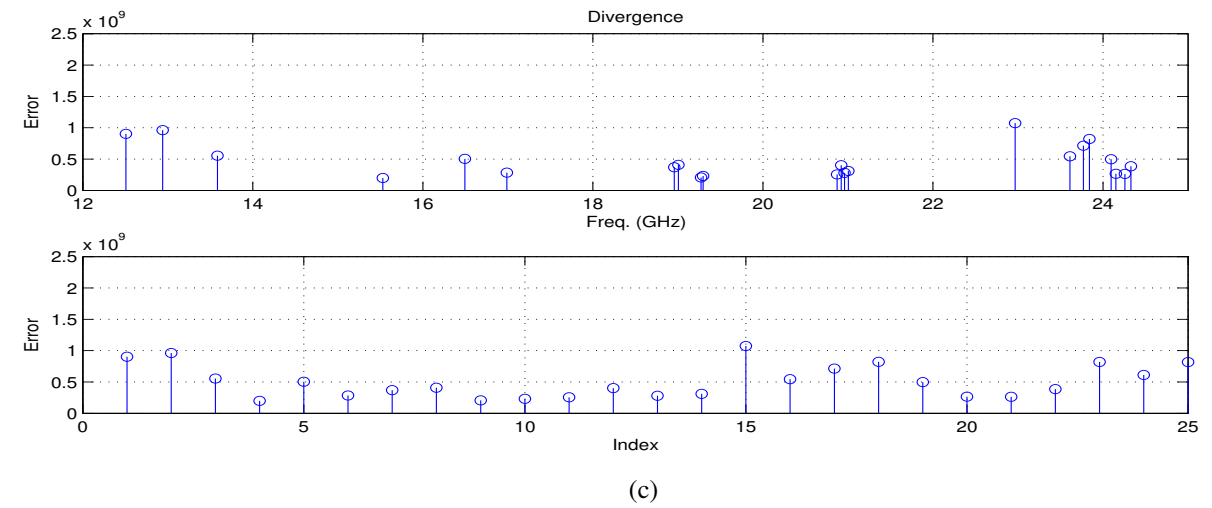
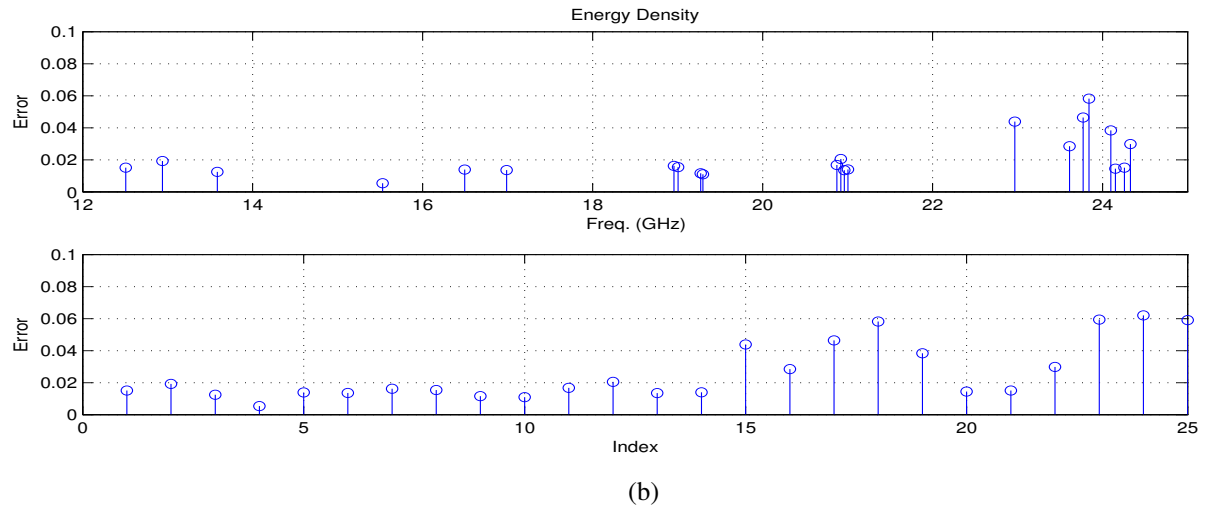
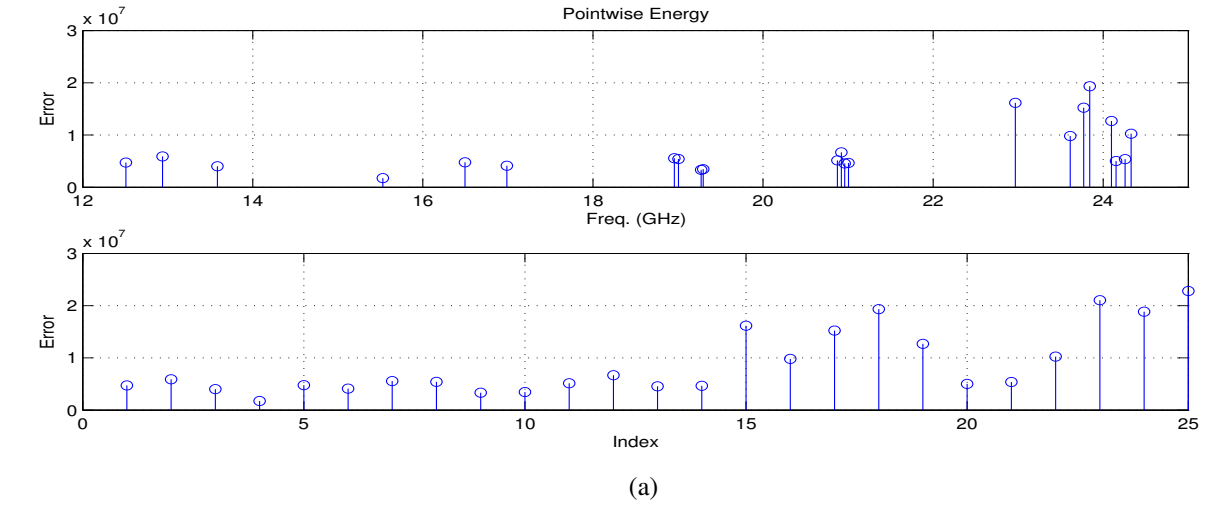


Figure 4.25 Errors of 25 modes with spurious exclusion calculated by (a) Point-wise energy (b) Energy density (c) Divergence obtained from perturbation

CHAPTER FIVE

CONCLUSION

Resonant structures are essential components for microwave applications. Among various alternatives for different applications, the cavity resonators are one of the widely used passive elements due to their superior quality factor and ease of construction. Performing optimization, tuning and sensitivity analysis on these structures corresponds to the perturbation of a parameter (e.g. permittivity, dimension etc.), assuming that the initial solutions exist already. Initial solution of the problem can be obtained by FEM, which leads to the generalized eigenvalue/eigenvector problem for cavity analysis. Then, the perturbation can be applied upon the solutions of the eigenvalue problem by means of classical eigenvalue perturbation techniques as long as the amount of perturbation is relatively small. However, this criteria is not always satisfied, hence, multiple FEM solutions are required as each step of variation brings a new eigenvalue problem to be solved. Consequently, the process becomes computationally demanding since typical FEM problems may involve several thousand variables. In order to reduce the computational requirements, the step-by-step eigenvalue perturbation technique can be used where the variation is divided into smaller steps and each new solution is calculated as linear combination of the previous solution. This also provides a parametric history of the process, which is useful to track down the solution for certain criteria. Effectiveness of step-by-step perturbation method has been recently shown by (Günel & Zoral, 2014) where the initial solutions are obtained by the vector FEM. Although the vector FEM is widely used today, its formulation requires complex geometrical data to be handled. Therefore, traditional nodal FEM is occasionally more preferable. It can be said that though, the performance of the step-by-step perturbation technique would be different for nodal FEM, compared to the vector FEM case, due to the spurious modes which occurs more seriously in nodal FEM. In order to examine the performance of the method under nodal FEM, a software, which includes the step-by-step perturbation algorithm as well as nodal FEM routine, is created using Python language. Partially filled cubic cavities are examined as the test cases due to having analytical solutions. Both the FEM routine and the step-by-step perturbation algorithm are tested with different parameters and the effects of these parameters over the solutions are investigated thoroughly.

First of all, two FEM parameters, the mesh resolution and the divergence coefficient are examined. It is observed that the mesh resolution increases the accuracy in the expense of the computational cost. Test cases involved 3500 variables in the resulting

eigenvalue problem, which is solved in several minutes using linear algebra libraries written in FORTRAN. On the other hand, introducing the divergence term in the formulation helps to distinguish the spurious modes, to a certain degree.

Analysis of the step-by-step perturbation technique is more complicated as it not only involves the examination of the parameters (number of steps, vectors to be perturbed) but also certain limitations about the process. Experiments on the effects of the number of steps revealed that the average error differs by a very small amount for different stepping schemes. This is the result of solving a reduced eigenvalue problem at each step. However, dividing the process into smaller steps helps for observing the parametric history. It has been pointed out that selecting the correct eigenvalue and matching it with the correct mode configuration is vital for tracking as it is possible that two different perturbed eigenvalues might align with the analytical solution, for different parts of the process. This points out another vital fact, which is the corruption caused by the crossings between eigenvalues when the perturbation is large. It can be concluded that, the higher number of perturbation steps is useful for detecting any abnormal deviation if the total amount of perturbation is large. The parts where the perturbation and analytical curves align, the average error is as low as %2.

On the next stage, the effects of the number of the eigenvalues used in perturbation is investigated. The results showed that the average error can be reduced significantly by increasing the number of the tracked eigenvalues. The tracked eigenvalues are chosen from those with lowest values, including many spurious modes as well.

Finally, an elimination is made on the eigenvalues to be selected by investigating their errors. Three error criteria, namely point-wise energy, energy density and divergence error, are used for this elimination. Improvements in the perturbation results are also examined by using these criteria. Eliminating even only a few eigenvalues has resulted in significant improvement. Ultimately, the accuracy of the step-by-step perturbation method can be increased in the case of nodal FEM by pre-processing the solutions against the spurious modes. This also eases the matching efforts of correct eigenvalues with corresponding modes.

REFERENCES

- Bai, Z., Demmel, J., Dongarra, J., Ruhe, A., & Vorst, H. van der, (Eds.) (2000). *Templates for the solution of algebraic eigenvalue problems: a practical guide*. SIAM, Philadelphia.
- Balanis, C.A. (1989). *Advanced engineering electromagnetics*. NJ: Wiley.
- Calvetti, D., Reichel, D., & Sorensen, D.C. (1994). An implicitly restarted Lanczos method for large symmetric eigenvalue problem. *Electronic Transactions on Numerical Analysis*, 2, 1–21.
- Carter, R. (2001). Accuracy of microwave cavity perturbation measurements. *IEEE Transactions on Microwave Theory and Techniques*, 49 (5), 918–923.
- Cendes, Z. (1991). Vector finite elements for electromagnetic field computations. *IEEE Transactions on Magnetics*, 27 (5), 3958–3966.
- Collin, R.E. (1990). *Field theory of guided waves*. (2nd ed.) Wiley-IEEE Press.
- Collin, R.E. (1992). *Foundations for microwave engineering*. (2nd ed.) NY: McGraw Hill.
- Geuzaine, C. & Remacle, J.-F. (2009). Gmsh: a three-dimensional finite element mesh generator with built-in pre- and post-processing facilities. *International Journal for Numerical Methods in Engineering*, 79 (11), 1309–1331.
- Golub, G.H. & Van Loan, C.F. (1996). *Matrix Computations*. (3rd ed.) Johns Hopkins University Press.
- Gunel, S. & Zoral, Y. (2010). Parametric history analysis of resonance problems via step-by-step eigenvalue perturbation technique. *IET Microwaves Antennas & Propagation*, 4 (4), 466–476.
- Gunel, S. & Zoral, Y. (2012). *Elektromanyetik rezonans problemlerinin parametrik geçmiş çözümlemesinde sonlu elemanlar ve adım adım özdeğer pertürbasyonu problemine indirgenmesi*. Technical Report. Dokuz Eylül Üniversitesi.

- Gunel, S. & Zoral, Y. (2014). Vector finite elements and the step by step eigenvalue perturbation methods. *Journal of Physics: Conference Series*, 490 (1).
- Harrington, R.F. (2001). *Time harmonic electromagnetic fields*. (2nd ed.) Wiley-IEEE Press.
- Horn, R.A. & Johnson, C.R. (1985). *Matrix Analysis*. Cambridge University Press.
- Ise, K., Inoue, K., & Koshiba, M. (1990). Three-dimensional finite-element solution of dielectric scattering obstacles in a rectangular waveguide. *IEEE Transactions on Microwave Theory and Techniques*, 38 (9), 1352–1359.
- Jin, J. (2002). *The finite element method in electromagnetics*. (2nd ed.) Wiley.
- Lee, J. F. & Mittra, R. (1992). A note on the application of edge-elements for modeling three-dimensional inhomogeneously filled cavities. *IEEE Transactions on Microwave Theory and Techniques*, 40 (9), 1767–1773.
- Logan, D.L. (2011). *A first course in the finite element method*. (5th ed.) Cengage Learning.
- Lu, Z.H., Shao, C., & Feng, Z.D. (1993). High accuracy step-by-step perturbation method of the generalized eigenvalue problem and its application to the parametric history analysis of structural vibration characteristics. *Journal of Sound and Vibration*, 164 (3), 459–469.
- Mabaya, N., Lagasse, P.E., & Vandenbulcke, P. (1981). Finite element analysis of optical waveguides. *IEEE Transactions on Microwave Theory and Techniques*, 29 (6), 600–605.
- Oliphant, T.E. (2007). Python for scientific computing. *Computing in Science & Engineering*, 9 (90).
- Price, R., Reed, R., & Roberts, C. (1963). Perturbation theory for resonant cavities. *IEEE Transactions on Antennas and Propagation*, 11 (5), 587.
- Rahman, B. & Davies, J. (1984). Penalty function improvement of waveguide solution by finite elements. *IEEE Transactions on Microwave Theory and Techniques*, 32 (8), 922–928.

- Rahman, B.M.A., Fernandez, F.A., & Davies, J.B. (1991). Review of the finite element method for microwave and optical waveguides. *Proceedings of the IEEE*, 79 (10), 1442–1448.
- Spencer, E. G., LeCraw, R. C., & Ault, L. A. (1957). Note on cavity perturbation theory. *Journal of Applied Physics*, 28 (1), 130–132.
- Stewart, G.W. & Sun, J. (1990). *Matrix perturbation theory*. Academic Press Inc.
- Sun, D., Manges, J., Yuan, X., & Cendes, Z. (1995). Spurious modes in finite-element method. *IEEE Antennas and Propagation Magazine*, 37 (5), 12–24.
- Van Bladel, J. (2007). *Electromagnetic fields*. (2nd ed.) Wiley-IEEE Press.
- Wang, J. S. & Ida, N. (1992). Eigenvalue analysis in anisotropically loaded electromagnetic cavities using edge finite elements. *IEEE Transactions on Magnetics*, 28 (2), 1438–1441.
- Wilson, J.K. (1984). A new element bisection algorithm for unstructured adaptive tetrahedral mesh generation. *Engineering Computations*, 15 (5), 588–615.
- Zaki, K.A. & Atia, A.E. (1983). Modes in dielectric-loaded waveguides and resonators. *IEEE Transactions on Microwave Theory and Techniques*, 31 (12), 1039–1045.